

1
2 **Munc13 supports vesicle fusogenicity after disrupting active zone scaffolds and synaptic**
3 **vesicle docking**

4
5
6
7
8 Chao Tan¹, Giovanni de Nola¹, Claire Qiao¹, Cordelia Imig^{2,3}, Nils Brose³, and Pascal S.
9 Kaeser^{1,#}

10
11
12
13 ¹Department of Neurobiology, Harvard Medical School, Boston, MA 02115, USA.
14 ²Department of Neuroscience, University of Copenhagen, 2200 Copenhagen, Denmark
15 ³Department of Molecular Neurobiology, Max Planck Institute for Multidisciplinary Sciences, City
16 Campus, 37075 Göttingen, Germany
17
18 #Correspondence: kaeser@hms.harvard.edu
19

20 **Abstract**

21
22 Presynaptic active zones consist of protein scaffolds that are tightly attached to the target
23 plasma membrane. They dock and prime synaptic vesicles, couple them to Ca^{2+} entry, and
24 direct neurotransmitter release towards postsynaptic receptor domains. Simultaneous
25 RIM+ELKS ablation disrupts these scaffolds, abolishes vesicle docking and removes active
26 zone-targeted Munc13, but some vesicles remain releasable. This enduring vesicular
27 fusogenicity may be Munc13-independent or be mediated by non-active zone-anchored Munc13.
28 We tested its Munc13-dependence by ablating Munc13-1 and Munc13-2 on top of RIM+ELKS in
29 mouse hippocampal neurons. The hextuple knockout synapses lacked docked vesicles, but
30 other ultrastructural features were near-normal despite the strong genetic manipulation.
31 Removing Munc13 in addition to RIM+ELKS impaired action potential-evoked release more
32 strongly than RIM+ELKS knockout by further decreasing the releasable vesicle pool. Hence,
33 Munc13 can support some fusogenicity without RIM and ELKS, and presynaptic recruitment of
34 Munc13, even without active zone-anchoring, suffices to generate some fusion-competent
35 vesicles.

36

37 **Introduction**

38

39 Neurotransmitter release is mediated by synaptic vesicle fusion at presynaptic active zones, and
40 Munc13 proteins have a central role in this process (Brunger et al., 2018; Dittman, 2019; Wojcik
41 and Brose, 2007). In addition to Munc13, active zone scaffolds contain RIM, ELKS, RIM-BP,
42 Bassoon/Piccolo, and Liprin- α . Together, they form a protein machine that controls the speed
43 and precision of synaptic transmission by docking and priming of synaptic vesicles, by
44 organizing their coupling to sites of Ca^{2+} entry, and by targeting transmitter release towards
45 postsynaptic receptor domains (Biederer et al., 2017; Südhof, 2012). Given the molecular
46 complexity of the active zone, understanding its assembly and functions has remained a key
47 challenge in synaptic neuroscience.

48

49 Mouse knockout studies established a major role of Munc13 in vesicle priming at central
50 nervous synapses (Augustin et al., 1999; Varoqueaux et al., 2002). This process renders
51 vesicles fusion-competent and adds them to the pool of readily releasable vesicles (RRP) that
52 can rapidly undergo exocytosis upon action potential arrival. The functional RRP can be probed
53 experimentally by applying stimuli that deplete it, for example superfusion of hypertonic sucrose
54 (Kaeser and Regehr, 2017; Rosenmund and Stevens, 1996). When Munc13 is deleted, release-
55 competence of vesicles is abolished or strongly decreased across all tested synapses in
56 multiple model organisms, including mouse, *Drosophila melanogaster* and *Caenorhabditis*
57 *elegans* (Aravamudan et al., 1999; Augustin et al., 1999; Richmond et al., 1999; Varoqueaux et
58 al., 2002). Munc13 ablation also results in an almost complete loss of docked vesicles, as
59 defined by plasma membrane attachment in electron micrographs (Hammarlund et al., 2007;
60 Imig et al., 2014; Sikorski et al., 2009). These findings led to the model that vesicle docking and
61 priming are morphological and functional states that correspond to release competence, which
62 is further supported by similar correlations upon ablation of SNARE proteins (Chen et al., 2021;

63 Hammarlund et al., 2007; Imig et al., 2014; Kaeser and Regehr, 2017). Due to their core
64 function in vesicle priming, Munc13 mediates the resupply of fusion-competent vesicles as they
65 are spent during synaptic activity and thereby controls short-term plasticity and recovery from
66 depression (Lipstein et al., 2013, 2021; Rosenmund et al., 2002). Furthermore, Munc13 nano-
67 assemblies may account for secretory hotspots and recruit the SNARE protein syntaxin-1
68 (Reddy-Alla et al., 2017; Sakamoto et al., 2018).

69

70 Several recent studies took the approach to ablate combinations of active zone protein families
71 for analyzing active zone assembly and function through eliminating redundant components
72 (Acuna et al., 2016; Brockmann et al., 2020; Kushibiki et al., 2019; Oh et al., 2021; Tan et al.,
73 2022; Wang et al., 2016; Zarebidaki et al., 2020). We simultaneously deleted RIM1, RIM2,
74 ELKS1 and ELKS2, which resulted in a loss of RIM, ELKS, and Munc13, and in strong
75 decreases of Bassoon, Piccolo, and RIM-BP levels at active zones (Tan et al., 2022; Wang et
76 al., 2016; Wong et al., 2018). This disruption of active zone assembly led to a near-complete
77 loss of synaptic vesicle docking as studied by electron microscopy and to an ~85% decrease in
78 single action potential-evoked exocytosis as assessed electrophysiologically. However, some
79 transmitter release persisted: up to ~35% of release evoked by hypertonic sucrose and ~50% of
80 spontaneous release events remained under the tested experimental conditions, increasing
81 extracellular Ca^{2+} to increase vesicular release probability p strongly enhanced single action
82 potential-evoked release, and stimulus trains released vesicles quite efficiently (Wang et al.,
83 2016). Hence, some releasable vesicles persisted despite the loss of most docked vesicles.
84 These findings supported alternative mechanistic models in which docking and priming are
85 independent processes mediated by distinct molecular functions of Munc13 (Kaeser and
86 Regehr, 2017). Further support for this model came from experiments with artificial re-targeting
87 of Munc13 to synaptic vesicles rather than to active zones, which increased vesicle fusogenicity
88 but not docking in mutants that lack most RIM and ELKS sequences and docked vesicles (Tan

89 et al., 2022). Together, these findings indicate that non-docked vesicles can contribute to the
90 functional RRP after removal of RIM and ELKS. What remained enigmatic, particularly in view of
91 the near-complete loss of Munc13 from the target membrane after RIM+ELKS ablation, was
92 whether undocked vesicles engaged Munc13 for vesicle priming or used an alternative priming
93 pathway.

94

95 In the present study, we tested directly whether Munc13 is sufficient to prime vesicles after the
96 strong active zone disruption upon RIM+ELKS knockout. We generated mice for ablating
97 Munc13-1 and Munc13-2 in addition to RIM and ELKS (that is RIM1, RIM2, ELKS1 and ELKS2)
98 and compared phenotypes of hextuple knockout neurons generated from these mice with those
99 from conditional RIM+ELKS knockouts only. We find that synapses form despite this strong
100 genetic manipulation and that overall, their ultrastructure is largely normal except for a lack of
101 docked vesicles. However, Munc13 ablation on top of RIM and ELKS knockout further impaired
102 single action potential-evoked release and decreased the RRP at both excitatory and inhibitory
103 synapses. Paired pulse ratios, used to monitor p, were not further affected by the additional
104 removal of Munc13. Our data establish that Munc13 can functionally prime some vesicles in the
105 absence of RIM and ELKS, indicate that Munc13 away from active zones is sufficient to
106 enhance vesicle fusogenicity, and support a growing body of data showing that synapse
107 formation is overall remarkably resilient to severe perturbations of synaptic protein content and
108 of synaptic activity. We propose that Munc13 recruitment to presynapses is rate-limiting to
109 generate fusion competence of synaptic vesicles.

110

111 **Results**

112

113 **Some synaptic Munc13 remains after RIM+ELKS knockout**

114 With the overall goal to determine whether Munc13 mediates addition of vesicles to the
115 functional RRP after RIM+ELKS knockout, we first confirmed key effects on synaptic
116 transmission and Munc13 active zone levels in cultured neurons after ablation of RIM+ELKS
117 (Figs. 1) that we had described before (Tan et al., 2022; Wang et al., 2016). We cultured
118 primary hippocampal neurons of mice with floxed (fl) alleles for RIM1, RIM2, ELKS1 and ELKS2
119 (Fig. 1A). At 5 days in vitro (DIV5), a time point that is before the detection of functional
120 synapses in these cultures (Held et al., 2020; Mozhayeva et al., 2002), the neurons were
121 transduced with Cre-expressing lentiviruses or control lentiviruses (that express an inactive
122 mutant of cre) to generate cKO^{R+E} neurons or control^{R+E} neurons, respectively. We previously
123 established that this induces strong defects in active zone assembly and neurotransmitter
124 release, but the neurons form synapses at normal numbers, and postsynaptic receptor
125 assemblies and functions are preserved (Tan et al., 2022; Wang et al., 2016). We first
126 confirmed that excitatory and inhibitory synaptic transmission are strongly impaired in cKO^{R+E}
127 neurons (Figs. 1B-1F). Synaptic responses were induced by focal electrical stimulation, and
128 whole-cell recordings served to monitor excitatory and inhibitory transmission via glutamate and
129 GABA_A receptors (GABA_{AR}s), respectively. Action potential-evoked excitatory transmission was
130 monitored via NMDA receptors to prevent the strong reverberant activity that is induced by
131 stimulation of these neuronal networks when AMPA receptors (AMPARs) are not blocked.

132

133 We next evaluated Munc13-1 positioning and levels at the active zone using stimulated
134 emission depletion (STED) superresolution microscopy (Figs. 1G-1K). We stained for
135 Synaptophysin to mark the synaptic vesicle cloud (imaged by confocal microscopy), PSD-95 to
136 mark the postsynaptic density (PSD, imaged by STED), and Munc13-1 (imaged by STED). In

137 these experiments, side-view synapses are defined as a synaptic vesicle cluster with an
138 elongated PSD-95 structure aligned at one side of the vesicle cloud as described before
139 (Emperador-Melero et al., 2021a; Held et al., 2020; Nyitrai et al., 2020; Tan et al., 2022; Wong
140 et al., 2018). To evaluate Munc13-1 levels in the active zone area, we quantified PSD-95 and
141 Munc13-1 fluorescence levels in 200 x 600 nm line profiles that were positioned perpendicular
142 to the PSD through the center of the PSD-95 signal, and plotted both their line profiles (Figs. 1H,
143 1I) and peak levels (Figs. 1J, 1K). In this analysis, Munc13-1 was largely lost from the active
144 zone area of cKO^{R+E} synapses, while PSD-95 was unchanged.

145

146 For comparison, we pursued analyses of Munc13-1 levels at the active zone after ablation of
147 Munc13. We used mice with floxed alleles for Munc13-1 and constitutive knockout alleles for
148 Munc13-2 and Munc13-3 (Fig. 1 – figure supplement 1A) (Augustin et al., 2001; Banerjee et al.,
149 2022; Varoqueaux et al., 2002). In cultured neurons of these mice, Cre-expression removes
150 Munc13-1 (cKO^M) without the potential for compensation by Munc13-2 or -3 because these
151 genes are knocked out constitutively. Control experiments were performed on the same cultures
152 but with expressing a lentivirus with an inactive Cre (control^M). Munc13-1 was ablated efficiently
153 in cKO^M neurons (Fig. 1 – figure supplements 1B-1F), with the leftover signal not distinguishable
154 from background levels that are typically observed in this approach (Held et al., 2020; Nyitrai et
155 al., 2020; Wong et al., 2018). When we compared Munc13-1 levels in cKO^{R+E} and cKO^M
156 synapses, the remaining signal was somewhat higher in cKO^{R+E} synapses (Fig. 1 – figure
157 supplement 1G). These higher levels did not arise from a peak at the position of the active zone
158 area (around -70 to -20 nm) (Tan et al., 2022; Wong et al., 2018). Instead, Munc13-1 levels
159 appeared broadly increased, and the ratio of Munc13-1 at cKO^{R+E} vs. cKO^M synapses shifted
160 upwards throughout the presynaptic bouton (Fig. 1 – figure supplement 1G). In both types of
161 neurons, Synaptophysin signals remained unchanged (Fig. 1 – figure supplements 1H, 1I). As
162 observed before in autaptic cultures (Banerjee et al., 2022), there was some release left at

163 these Munc13 knockout synapses (Fig. 1 – figure supplement 2). This is likely due to the very
164 small amount of remaining Munc13-1 when using this conditional allele (Banerjee et al., 2022).

165

166 Because a small amount of remaining Munc13-1 could be detected in cKO^{R+E} neurons by STED
167 microscopy (Figs. 1G-1K, Fig. 1 – figure supplement 1G) and by Western blotting (Wang et al.,
168 2016), we compared synaptic Munc13-1 levels in cKO^{R+E} and cKO^M neurons (Fig. 1 – figure
169 supplement 3). There were somewhat higher Munc13-1 signals in confocal microscopic images
170 in cKO^{R+E} synapses compared to cKO^M synapses (Fig. 1 – figure supplements 3A, 3B, 3D, 3E).
171 Similarly, a slight Munc13-1 band was detected in Western blotting of cKO^{R+E} neurons, but not
172 in cKO^M neurons (Fig. 1 – figure supplements 3C, 3F). The remaining Munc13-1 signal in
173 immunostainings detected in cKO^M neurons is likely mostly composed of antibody background
174 in these experiments, as quantifications are done without background subtraction and noise
175 levels of ~25% are common (Wang et al., 2016). Altogether, our data indicate that some
176 Munc13-1 might remain in nerve terminals of cKO^{R+E} synapses, but the remaining Munc13 is
177 not efficiently concentrated in the active zone area apposed to the PSD, supporting previous
178 work on RIM-mediated recruitment of Munc13 to the active zone (Andrews-Zwilling et al., 2006).

179

180 **Synapses form after deletion of Munc13 in addition to RIM and ELKS**

181 With the overall goal to test whether Munc13-1 mediates the remaining release in cKO^{R+E}
182 neurons, we crossed the conditional knockout mice for RIM1, RIM2, ELKS1 and ELKS2 to
183 conditional Munc13-1 and constitutive Munc13-2 knockout mice (Fig. 2A). Cultured hippocampal
184 neurons from these mice were infected with Cre-expressing or control lentiviruses at DIV5 to
185 generate cKO^{R+E+M} and control^{R+E+M} neurons, respectively, to remove Munc13 in addition to
186 RIM+ELKS (Fig. 2A). We first used STED microscopy to analyze the localization and levels of
187 PSD-95, RIM1 and Munc13-1 (Figs. 2B-2K). RIM1 and Munc13-1 were effectively removed from
188 active zones of cKO^{R+E+M} neurons, while PSD-95 signals were largely normal (Figs. 2B-2K, Fig.

189 2 – figure supplement 1A). The Munc13-1 signal that remained in STED experiments of cKO^{R+E}
190 neurons (Figs. 1I, 1K, Fig. 1 – figure supplement 1G) further decreased in cKO^{R+E+M} neurons
191 (Fig. 2 – figure supplement 1B). In confocal images, there was a further decrease of synaptic
192 Munc13-1 levels in cKO^{R+E+M} neurons compared to cKO^{R+E} neurons (Fig. 2 – figure supplements
193 1C-1E), and Munc13-1 was below detection threshold in Western blotting (Fig. 2 – figure
194 supplement 1F). Finally, Synaptophysin puncta number, size and intensity, analyzed with a
195 custom-written code to perform automatic two-dimensional segmentation for object detection
196 (Emperador-Melero et al., 2021a; Held et al., 2020; Liu, 2022; Liu et al., 2018), were
197 indistinguishable between control^{R+E+M} and cKO^{R+E+M} neurons (Figs. 2L-2O). This indicates that
198 synapse formation is intact in the absence of these active zone proteins. Similar results were
199 also observed when we analyzed synapses in neurons infected with Cre-expressing lentiviruses
200 at DIV2 (Fig. 2 – figure supplement 2) instead of DIV5.

201
202 We next analyzed synaptic ultrastructure using high pressure freezing followed by transmission
203 electron microscopy in the cultured neurons (Fig. 3), following established procedures (Tan et
204 al., 2022; Wang et al., 2016). In these analyses, docked synaptic vesicles are defined as
205 vesicles for which the electron density of the vesicular membrane merges with that of the
206 presynaptic plasma membrane, and less electron-dense space cannot be detected between the
207 two membranes. Simultaneous deletion of RIM, ELKS and Munc13 abolished vesicle docking
208 (Figs. 3A, 3B) similar to RIM+ELKS ablation (Tan et al., 2022; Wang et al., 2016). While bouton
209 size was unchanged (Fig. 3D), there were small decreases in vesicle numbers and mild
210 increases for PSD-95 length in cKO^{R+E+M} neurons (Figs. 3C, 3E). This might be caused by
211 homeostatic adaptations or by general roles of these proteins in synapse development, or be
212 coincidental. Altogether, however, the morphological analyses including STED, confocal and
213 electron microscopy establish that nerve terminals and synaptic appositions form and are
214 overall ultrastructurally near-normal (apart from a loss of docked vesicles) despite the strong

215 genetic manipulation with deletions of RIM1, RIM2, ELKS1, ELKS2, Munc13-1 and Munc13-2.

216

217 **Deletion of Munc13 in addition to RIM and ELKS further impairs synaptic vesicle release**

218 Using whole-cell recordings, we then assessed synaptic transmission in cKO^{R+E+M} neurons and
219 corresponding controls. We first measured spontaneous vesicle release by assessing miniature
220 excitatory and inhibitory postsynaptic currents (mEPSCs and mIPSCs, respectively) in the
221 presence of the sodium channel blocker tetrodotoxin. The frequencies of mEPSCs and mIPSCs
222 were robustly decreased in cKO^{R+E+M} neurons, while their amplitudes remained unchanged
223 (Figs. 4A-4F). In addition, there was a small increase of mEPSC rise times, similar to cKO^{R+E}
224 neurons (Tan et al., 2022), while mEPSC decay times and mIPSC kinetics were unchanged (Fig.
225 4 – figure supplement 1). Hence, vesicle release is impaired, but postsynaptic neurotransmitter
226 detection is fundamentally intact in cKO^{R+E+M} neurons.

227

228 We then measured single action potential-evoked release at cKO^{R+E+M} synapses (Figs. 4G-4K).
229 The cKO^{R+E+M} neurons had very strong reductions in evoked release, both at excitatory (Figs.
230 4G, 4H) and inhibitory (Figs. 4I-4K) synapses compared to control^{R+E+M} neurons. To directly
231 compare this reduction to that observed in cKO^{R+E} neurons (Figs. 1B-1E), we normalized the
232 cKO PSC amplitudes to their own controls, which are genetically identical except for the
233 expression of Cre recombinase. We then compared the normalized data across genotypes (Figs.
234 4L, 4M). This analysis established that for both excitatory and inhibitory synapses, Munc13
235 knockout in addition to RIM+ELKS knockout decreased the remaining PSCs by ~40-50%
236 compared to RIM+ELKS knockout only. The remaining release in cKO^{R+E+M} neurons might be
237 due to the low amount of exon 21/22-deficient Munc13-1 that persists after conditional Munc13-1
238 1 knockout with this allele (Banerjee et al., 2022) (Fig. 1 – figure supplement 2), to Munc13-1
239 that persists beyond 11 days of Cre expression, to Munc13-3 that was not deleted in the
240 hextuple knockout mice, or to an alternative release pathway that does not depend on RIM,

241 ELKS and Munc13. Altogether, however, the data establish that the remaining synaptic
242 transmission after RIM and ELKS knockout depends at least partially on the presence of
243 Munc13-1 and Munc13-2.

244

245 **Munc13 contributes to a remaining functional RRP after active zone disruption**

246 Given the further reduction of synaptic transmission when Munc13 is ablated in cKO^{R+E} neurons,
247 we analyzed vesicle priming and release probability in cKO^{R+E+M} neurons. The goal was to
248 determine which release properties are controlled by Munc13 through comparison of these
249 parameters with cKO^{R+E} neurons. We assessed the functional RRP at both excitatory and
250 inhibitory synapses through the application of hypertonic sucrose, a method that has been
251 broadly used to evaluate correlations between vesicle docking and priming (Imig et al., 2014;
252 Rosenmund and Stevens, 1996; Wang et al., 2016; Zarebidaki et al., 2020). We detected robust
253 reductions of the vesicle pool assessed by this method for both AMPAR and GABA_{AR}-mediated
254 responses in cKO^{R+E} neurons (Figs. 5A-5D), but the functional RRP was not fully disrupted.
255 Deletion of Munc13 on top of RIM and ELKS revealed an additional decrease, with an almost
256 complete loss of releasable vesicles at excitatory cKO^{R+E+M} synapses and a >80% reduction at
257 inhibitory cKO^{R+E+M} synapses (Figs. 5E-5H). Comparison of these two genotypes by normalizing
258 each mutant to their corresponding control condition revealed that cKO^{R+E+M} neurons showed a
259 significantly smaller RRP size (Figs. 5I, 5J) than cKO^{R+E} synapses in both synapse types. We
260 conclude that the fusion-competence of vesicles that remains after active zone disruption by
261 RIM+ELKS knockout is mediated at least in part by Munc13. Because Munc13 is not active
262 zone-anchored and docked vesicles are barely detectable in cKO^{R+E} neurons, these vesicles
263 are undocked, but likely associated with Munc13 away from the active zone.

264

265 We finally used paired pulse ratios to monitor vesicular release probability p in control^{R+E+M} and
266 cKO^{R+E+M} neurons and repeated the measurements in cKO^{R+E} neurons for direct comparison

(Fig. 6). Paired pulse ratios are inversely correlated with p (Zucker and Regehr, 2002) and
strongly increased at short interstimulus intervals after knockout of RIM and ELKS at excitatory
and inhibitory synapses (Figs. 6A-6D) (Tan et al., 2022; Wang et al., 2016). In cKO^{R+E+M}
neurons, p was also strongly decreased, illustrated by robust increases in EPSC and IPSC
paired pulse ratios (Figs. 6E-6H), to an extent that is overall very similar to cKO^{R+E} neurons.
Direct comparison of genotypes through normalization supported the conclusion that Munc13
knockout in addition to RIM and ELKS did not further decrease p, as effects in cKO^{R+E} synapses
and in cKO^{R+E+M} synapses were indistinguishable (Figs. 6I, 6J). Consistent with this comparison,
spontaneous mEPSC and mIPSC frequencies (Fig. 6 – figure supplements 1A-1H) and
depression of IPSCs during stimulus trains (Fig. 6 – figure supplements 1I-1L) were similar in
the two genotypes. Hence, while the remaining Munc13 at cKO^{R+E} synapses is sufficient to
maintain a small functional RRP, it does not enhance vesicular release probability of these
vesicles.

280

281 **Discussion**

282

283 We found previously that the functional RRP is not fully disrupted after ablating vesicle docking
284 by simultaneous knockout of RIM and ELKS (Wang et al., 2016). Here, we show that fusion of
285 these remaining RRP vesicles depends at least in part on Munc13. Even though Munc13-1 is
286 not active zone-anchored after RIM and ELKS ablation, knocking out Munc13 in addition
287 decreases the remaining releasable vesicles at excitatory and inhibitory hippocampal synapses.
288 We conclude that Munc13 can render some vesicles fusogenic in the absence of RIM and ELKS.
289 Our work adds the strongest compound knockout mutation to disrupt synaptic function with
290 removal of six important active zone proteins to a growing body of literature using this approach.
291 Beyond its relevance for mechanisms of neurotransmitter release, our work supports that the
292 formation of synapses is remarkably resilient to even massive perturbations of presynaptic
293 function and protein composition.

294

295 **Disrupting active zones to remove redundancy**

296 Knockout studies on active zone gene families have defined multiple roles for these proteins in
297 the neurotransmitter release process. While some functions and mechanisms, for example
298 vesicle priming (Aravamudan et al., 1999; Augustin et al., 1999; Richmond et al., 1999;
299 Varoqueaux et al., 2002), strongly depend on single proteins, other functions are redundant
300 across protein families and hence more difficult to study mechanistically. This is particularly true
301 for the scaffolding mechanisms that hold the active zone together and connect it with the target
302 membrane and the vesicle cluster. These mechanisms are not well defined and models ranging
303 from self-assembly of complexes with defined stoichiometries to phase separation based on
304 multivalent low-affinity interactions have been proposed (Chen et al., 2020; Emperador-Melero
305 and Kaeser, 2020; Südhof, 2012). Recent studies with compound mutants that ablate
306 combinations of active zone protein families started to identify the required active zone scaffolds

307 (Acuna et al., 2016; Kushibiki et al., 2019; Oh et al., 2021; Wang et al., 2016). We found
308 previously that simultaneous deletion of RIM and ELKS in hippocampal neurons strongly
309 disrupts active zone protein assemblies with loss of Munc13, RIM-BP, Piccolo, and Bassoon
310 (Tan et al., 2022; Wang et al., 2016; Wong et al., 2018). This loss of active zone material
311 causes a near-complete disruption of vesicle docking, and strongly impaired action potential-
312 triggered release. Unexpectedly, however, some release persisted, either due to the presence
313 of remaining release-competent but non-docked vesicles, or due to the rapid generation of
314 release-competent vesicles in response to stimulation. The present study establishes that the
315 transmitter release that remains after RIM and ELKS deletion relies at least in part on Munc13,
316 as ablating Munc13 on top of RIM and ELKS robustly decreased the remaining functional RRP.
317 The remaining release in cKO^{R+E+M} neurons might be Munc13-independent, which is currently
318 not possible to establish, or perhaps more likely due to the small amount of remaining Munc13
319 protein in the mice used here (Banerjee et al., 2022) compared to earlier Munc13-1 mutants
320 (Augustin et al., 1999; Man et al., 2015). We further found that synapse structure per se is
321 resilient to this major genetic and functional perturbation, as synapses formed at normal
322 densities and showed overall normal ultrastructure despite the removal of six important active
323 zone genes in the cultured neurons. Our work adds to a growing body of data demonstrating
324 that neurotransmitter release, presynaptic Ca²⁺ entry, and active zone scaffolding are all
325 dispensable for the formation of prominent types of central nervous system synapses (Held et
326 al., 2020; Sando et al., 2017; Sigler et al., 2017; Verhage et al., 2000).

327
328 One way to interpret our data is to compare them with properties of fusion in other secretory
329 pathways. Synaptic vesicle exocytosis after RIM and ELKS knockout has resemblance with
330 secretion from chromaffin cells (Neher, 2018; Wang et al., 2016). In these cells, the release-
331 ready pool of vesicles depends on Munc13, has relatively slower kinetics compared to synapses,
332 but appears to not rely on the sequences of Munc13 that interact with RIM and on active zone

333 scaffolds more generally (Betz et al., 2001; Man et al., 2015; Neher, 2018). The similarities of
334 the remaining fusion after disrupting active zone assembly by knockout of RIM and ELKS are
335 striking in that the release kinetics appear slowed down (Wang et al., 2016), the remaining
336 fusion depends on Munc13 (Figs. 3-6), and docking and the functional RRP are not fully
337 correlated. Some of these similarities are also reminiscent of recent studies in *C. elegans*,
338 where vesicle priming does not rely on the interaction of unc-13/Munc13 with unc-10/RIM, and
339 possibly RIM itself (Liu et al., 2019). Altogether, these studies and our work indicate that
340 disrupting the active zone through RIM+ELKS knockout renders synaptic vesicle exocytosis
341 similar to chromaffin cell secretion. Notably, there are specific synapses with similar properties.
342 For example, at hippocampal mossy fiber synapses, strong depolarizations lead to RRP
343 estimates that are larger than the number of docked vesicles (Maus et al., 2020), supporting the
344 model that RRP vesicles can be rapidly generated and released during such stimuli, perhaps
345 similar to cKO^{R+E} synapses.

346

347 **Can Munc13 prime vesicles in the absence of RIM?**

348 Our data reveal that the transmitter release that remains after active zone disruption upon RIM
349 and ELKS deletion depends at least in part on Munc13. Thus, Munc13 might render some
350 vesicles fusion-competent in the absence of RIM and when Munc13 is not anchored at the
351 active zone. This mechanism, however, is inefficient, as it only maintains a fraction of the
352 functional RRP of a wild type synapse. An alternative model is that fusion-competence is rapidly
353 generated and immediately followed by exocytosis during pool-depleting stimuli. We recently
354 established that the functional RRP after RIM+ELKS knockout can be further boosted by re-
355 expressing RIM zinc finger domains without enhancing vesicle docking (Tan et al., 2022). The
356 zinc finger domain was co-localized with the vesicle cluster, was not concentrated at the active
357 zone, and recruited Munc13 to the vesicle cluster. Hence, Munc13 can enhance vesicle
358 fusogenicity through association with non-docked vesicles, at least when this association is

359 generated artificially. Here, we show that the remaining fusion in RIM+ELKS knockouts depends
360 on Munc13 (Figs. 4, 5), but that Munc13-1 is barely detectable at the active zone, while some
361 Munc13 is present at synapses. These data indicate that endogenous Munc13 can be near
362 vesicles and enhance their fusogenicity even if Munc13 is not active zone-anchored. Hence,
363 Munc13 on non-docked vesicles might mediate the remaining fusion through generation of a
364 pool of vesicles that can be rapidly primed and released upon stimulation. Altogether, a model
365 arises that the rate-limiting step for generation of a functional RRP is the presynaptic
366 recruitment of Munc13, even if Munc13 is not fully anchored and activated at the active zone.
367 Upon stimulation, roles of Munc13 in SNARE complex assembly and fusion can be executed
368 quickly.

369

370 Previous work established that RIM recruits Munc13 to active zones and activates it. This
371 mechanism operates through binding of the RIM zinc finger to Munc13 C₂A domains, which is
372 necessary for rendering Munc13 monomeric and active in fusion (Andrews-Zwilling et al., 2006;
373 Betz et al., 2001; Brockmann et al., 2020; Camacho et al., 2017; Deng et al., 2011; Dulubova et
374 al., 2005; Lu et al., 2006). In the experiments presented here, the release remaining in the
375 absence of RIM and ELKS depends on Munc13. This indicates that not all priming requires the
376 RIM-mediated activation-mechanism of Munc13, consistent with previous observations that
377 many but not all RRP vesicles are lost after RIM knockout (Han et al., 2011; Kaeser et al., 2011,
378 2012). An alternative mechanism could operate via bMunc13-2 (which lacks the C₂A-domain
379 that binds to RIM) and ELKS (Kawabe et al., 2017). While ELKS provides a Munc13-recruitment
380 and priming mechanism that is independent of RIM, most ELKS is also removed in the
381 RIM+ELKS knockout neurons (Kaeser et al., 2009; Liu et al., 2014; Wang et al., 2016), and only
382 a very small subset of synapses relies on bMunc13-2 (Kawabe et al., 2017). Hence, this
383 mechanism might be insufficient to explain the remaining release from RIM+ELKS knockout
384 neurons. An alternative and perhaps more likely explanation is that not all C₂A-domain

385 containing Munc13 requires RIM. Monomeric, active Munc13 is in equilibrium with dimeric,
386 inactive Munc13, and RIM shifts the equilibrium to the active form. Even in the absence of RIM,
387 some Munc13 will be monomeric and available for assembling SNARE complexes, accounting
388 for the vesicular exocytosis that remains in RIM+ELKS knockout neurons. Finally, this
389 mechanism may not be restricted to docked vesicles, but vesicles associated with Munc13 may
390 be amenable to release, explaining why some release persists in RIM+ELKS mutants despite
391 the loss of active zone-anchored Munc13 and of a strong reduction in docked vesicles.

392

393 **Acknowledgements**

394

395 We thank J. Wang and V. Charles for technical support, all members of the Kaeser laboratory
396 for insightful discussions and feedback, and M. Verhage and J. Broeke for a MATLAB macro to
397 analyze electron microscopic images. C. Q. is currently a graduate student at Peking University.

398 This work was supported by grants from the NIH (R01MH113349 and R01NS083898 to P.S.K.).

399 We acknowledge the Neurobiology Imaging Facility (supported by a P30 Core Center Grant
400 P30NS072030), and the Electron Microscopy Facility at Harvard Medical School.

401

402 **Declaration of interests**

403

404 The authors declare no competing interests. N.B. is a reviewing editor for eLife.

405

406

407

408

409

410

411

412

413 **References**

- 414 Acuna, C., Liu, X., and Südhof, T.C. (2016). How to Make an Active Zone: Unexpected
415 Universal Functional Redundancy between RIMs and RIM-BPs. *Neuron* 91, 792–807.
- 416 Andrews-Zwilling, Y.S., Kawabe, H., Reim, K., Varoqueaux, F., and Brose, N. (2006). Binding to
417 Rab3A-interacting molecule RIM regulates the presynaptic recruitment of Munc13-1 and
418 ubMunc13-2. *J. Biol. Chem.* 281, 19720–19731.
- 419 Aravamudan, B., Fergestad, T., Davis, W.S., Rodesch, C.K., and Broadie, K. (1999). Drosophila
420 UNC-13 is essential for synaptic transmission. *Nat. Neurosci.* 2, 965–971.
- 421 Augustin, I., Rosenmund, C., Südhof, T.C., and Brose, N. (1999). Munc13-1 is essential for
422 fusion competence of glutamatergic synaptic vesicles. *Nature* 400, 457–461.
- 423 Augustin, I., Korte, S., Rickmann, M., Kretzschmar, H.A., Sudhof, T.C., Herms, J.W., and Brose,
424 N. (2001). The cerebellum-specific Munc13 isoform Munc13-3 regulates cerebellar synaptic
425 transmission and motor learning in mice. *J. Neurosci.* 21, 10–17.
- 426 Banerjee, A., Imig, C., Balakrishnan, K., Kershberg, L., Lipstein, N., Uronen, R.-L., Wang, J.,
427 Cai, X., Benseler, F., Rhee, J.S., et al. (2022). Molecular and functional architecture of
428 striatal dopamine release sites. *Neuron* 110, 248–265.e9.
- 429 Betz, A., Thakur, P., Junge, H.J., Ashery, U., Rhee, J.S., Scheuss, V., Rosenmund, C., Rettig,
430 J., and Brose, N. (2001). Functional interaction of the active zone proteins Munc13-1 and
431 RIM1 in synaptic vesicle priming. *Neuron* 30, 183–196.
- 432 Biederer, T., Kaeser, P.S., and Blanpied, T.A. (2017). Transcellular Nanoalignment of Synaptic
433 Function. *Neuron* 96, 680–696.
- 434 Brockmann, M.M., Zarebidaki, F., Camacho, M., Grauel, M.K., Trimbuch, T., Südhof, T.C., and
435 Rosenmund, C. (2020). A Trio of Active Zone Proteins Comprised of RIM-BPs, RIMs, and
436 Munc13s Governs Neurotransmitter Release. *Cell Rep.* 32, 107960.
- 437 Brunger, A.T., Choi, U.B., Lai, Y., Leitz, J., and Zhou, Q. (2018). Molecular Mechanisms of Fast
438 Neurotransmitter Release. *Annu. Rev. Biophys.* 47, 469–497.
- 439 Camacho, M., Basu, J., Trimbuch, T., Chang, S., Pulido-Lozano, C., Chang, S.-S., Duluvova, I.,
440 Abo-Rady, M., Rizo, J., and Rosenmund, C. (2017). Heterodimerization of Munc13 C2A
441 domain with RIM regulates synaptic vesicle docking and priming. *Nat. Commun.* 8, 15293.
- 442 Chen, X., Wu, X., Wu, H., and Zhang, M. (2020). Phase separation at the synapse. *Nat.*
443 *Neurosci.* 23, 301–310.
- 444 Chen, Y., Wang, Y.-H., Zheng, Y., Li, M., Wang, B., Wang, Q.-W., Fu, C.-L., Liu, Y.-N., Li, X.,
445 and Yao, J. (2021). Synaptotagmin-1 interacts with PI(4,5)P₂ to initiate synaptic vesicle
446 docking in hippocampal neurons. *Cell Rep.* 34, 108842.
- 447 Deng, L., Kaeser, P.S., Xu, W., and Südhof, T.C. (2011). RIM proteins activate vesicle priming
448 by reversing autoinhibitory homodimerization of Munc13. *Neuron* 69, 317–331.
- 449 Dittman, J.S. (2019). Unc13: a multifunctional synaptic marvel. *Curr. Opin. Neurobiol.* 57, 17–25.
- 450 Dulubova, I., Lou, X., Lu, J., Hurayeva, I., Alam, A., Schneggenburger, R., Sudhof, T.C., and Rizo,
451 J. (2005). A Munc13/RIM/Rab3 tripartite complex: from priming to plasticity? *EMBO J.* 24,
452 2839–2850.
- 453 Emperador-Melero, J., and Kaeser, P.S. (2020). Assembly of the presynaptic active zone. *Curr.*
454 *Opin. Neurobiol.* 63, 95–103.
- 455 Emperador-Melero, J., Wong, M.Y., Wang, S.S.H., de Nola, G., Nyitrai, H., Kirchhausen, T., and
456 Kaeser, P.S. (2021a). PKC-phosphorylation of Liprin- α 3 triggers phase separation and
457 controls presynaptic active zone structure. *Nat. Commun.* 12, 3057.
- 458 Emperador-Melero, J., de Nola, G., and Kaeser, P.S. (2021b). Intact synapse structure and
459 function after combined knockout of PTP δ , PTP σ and LAR. *Elife* 2021.01.17.427005.
- 460 Hammarlund, M., Palfreyman, M.T., Watanabe, S., Olsen, S., and Jorgensen, E.M. (2007).
461 Open syntaxin docks synaptic vesicles. *PLoS Biol.* 5, e198.
- 462 Han, Y., Kaeser, P.S., Südhof, T.C., and Schneggenburger, R. (2011). RIM determines Ca²⁺

- channel density and vesicle docking at the presynaptic active zone. *Neuron* 69, 304–316.
- Held, R.G., Liu, C., Ma, K., Ramsey, A.M., Tarr, T.B., De Nola, G., Wang, S.S.H., Wang, J., van den Maagdenberg, A.M.J.M., Schneider, T., et al. (2020). Synapse and Active Zone Assembly in the Absence of Presynaptic Ca²⁺ Channels and Ca²⁺ Entry. *Neuron* 107, 667–683.e9.
- Imig, C., Min, S.W., Krinner, S., Arancillo, M., Rosenmund, C., Südhof, T.C., Rhee, J.S., Brose, N., and Cooper, B.H. (2014). The Morphological and Molecular Nature of Synaptic Vesicle Priming at Presynaptic Active Zones. *Neuron* 84, 416–431.
- de Jong, A.P.H., Roggero, C.M., Ho, M.-R., Wong, M.Y., Brautigam, C.A., Rizo, J., and Kaeser, P.S. (2018). RIM C2B Domains Target Presynaptic Active Zone Functions to PIP2-Containing Membranes. *Neuron* 98, 335–349.e7.
- Kaeser, P.S., and Regehr, W.G. (2017). The readily releasable pool of synaptic vesicles. *Curr. Opin. Neurobiol.* 43, 63–70.
- Kaeser, P.S., Kwon, H.B., Chiu, C.Q., Deng, L., Castillo, P.E., and Sudhof, T.C. (2008). RIM1alpha and RIM1beta are synthesized from distinct promoters of the RIM1 gene to mediate differential but overlapping synaptic functions. *J. Neurosci.* 28, 13435–13447.
- Kaeser, P.S., Deng, L., Chávez, A.E., Liu, X., Castillo, P.E., and Südhof, T.C. (2009). ELKS2alpha/CAST deletion selectively increases neurotransmitter release at inhibitory synapses. *Neuron* 64, 227–239.
- Kaeser, P.S., Deng, L., Wang, Y., Dulubova, I., Liu, X., Rizo, J., and Südhof, T.C. (2011). RIM proteins tether Ca²⁺ channels to presynaptic active zones via a direct PDZ-domain interaction. *Cell* 144, 282–295.
- Kaeser, P.S., Deng, L., Fan, M., and Sudhof, T.C. (2012). RIM genes differentially contribute to organizing presynaptic release sites. *Proc. Natl. Acad. Sci.* 109, 11830–11835.
- Kawabe, H., Mitkovski, M., Kaeser, P.S., Hirrlinger, J., Opazo, F., Nestvogel, D., Kalla, S., Fejtová, A., Verrier, S.E.S.E., Bungers, S.R.S.R., et al. (2017). ELKS1 localizes the synaptic vesicle priming protein bMunc13-2 to a specific subset of active zones. *J. Cell Biol.* 216, 1143–1161.
- Kushibiki, Y., Suzuki, T., Jin, Y., and Taru, H. (2019). RIMB-1/RIM-Binding Protein and UNC-10/RIM Redundantly Regulate Presynaptic Localization of the Voltage-Gated Calcium Channel in *Caenorhabditis elegans*. *J. Neurosci.* 39, 8617–8631.
- Lipstein, N., Sakaba, T., Cooper, B.H., Lin, K.-H., Strenzke, N., Ashery, U., Rhee, J.-S., Taschenberger, H., Neher, E., and Brose, N. (2013). Dynamic control of synaptic vesicle replenishment and short-term plasticity by Ca(2+)-calmodulin-Munc13-1 signaling. *Neuron* 79, 82–96.
- Lipstein, N., Chang, S., Lin, K.-H., López-Murcia, F.J., Neher, E., Taschenberger, H., and Brose, N. (2021). Munc13-1 is a Ca²⁺-phospholipid-dependent vesicle priming hub that shapes synaptic short-term plasticity and enables sustained neurotransmission. *Neuron* 109, 3980–4000.e7.
- Liu, C. (2022). Matlab script for object recognition and analysis. Zenodo doi: 10.5281/zenodo.6342367; Version 1.
- Liu, C., Bickford, L.S., Held, R.G., Nyitrai, H., Südhof, T.C., and Kaeser, P.S. (2014). The active zone protein family ELKS supports Ca²⁺ influx at nerve terminals of inhibitory hippocampal neurons. *J. Neurosci.* 34, 12289–12303.
- Liu, C., Kershberg, L., Wang, J., Schneeberger, S., and Kaeser, P.S. (2018). Dopamine Secretion Is Mediated by Sparse Active Zone-like Release Sites. *Cell* 172, 706–718.e15.
- Liu, C., Cai, X., Ritzau-Jost, A., Kramer, P.F., Li, Y., Khalil, Z.M., Hallermann, S., and Kaeser, P.S. (2022). An action potential initiation mechanism in distal axons for the control of dopamine release. *Science* 375, 1378–1385.
- Liu, H., Li, L., Nedelcu, D., Hall, Q., Zhou, L., Wang, W., Yu, Y., Kaplan, J.M., and Hu, Z. (2019). Heterodimerization of UNC-13/RIM regulates synaptic vesicle release probability but not

- 514 priming in *C. elegans*. *Elife* 8.
- 515 Lu, J., Machius, M., Dulubova, I., Dai, H., Sudhof, T.C., Tomchick, D.R., and Rizo, J. (2006).
516 Structural basis for a Munc13-1 homodimer to Munc13-1/RIM heterodimer switch. *PLoS Biol.*
517 4, e192.
- 518 Man, K.N.M., Imig, C., Walter, A.M., Pinheiro, P.S., Stevens, D.R., Rettig, J., Sørensen, J.B.,
519 Cooper, B.H., Brose, N., and Wojcik, S.M. (2015). Identification of a Munc13-sensitive step
520 in chromaffin cell large dense-core vesicle exocytosis. *Elife* 4.
- 521 Maus, L., Lee, C., Altas, B., Sertel, S.M., Weyand, K., Rizzoli, S.O., Rhee, J., Brose, N., Imig, C.,
522 and Cooper, B.H. (2020). Ultrastructural Correlates of Presynaptic Functional Heterogeneity
523 in Hippocampal Synapses. *Cell Rep.* 30, 3632-3643.e8.
- 524 Mozhayeva, M.G., Sara, Y., Liu, X., and Kavalali, E.T. (2002). Development of vesicle pools
525 during maturation of hippocampal synapses. *J. Neurosci.* 22, 654–665.
- 526 Neher, E. (2018). Neurosecretion: what can we learn from chromaffin cells. *Pflugers Arch.* 470,
527 7–11.
- 528 Nyitrai, H., Wang, S.S.H., and Kaeser, P.S. (2020). ELKS1 Captures Rab6-Marked Vesicular
529 Cargo in Presynaptic Nerve Terminals. *Cell Rep.* 31, 107712.
- 530 Oh, K.H., Krout, M.D., Richmond, J.E., and Kim, H. (2021). UNC-2 CaV2 Channel Localization
531 at Presynaptic Active Zones Depends on UNC-10/RIM and SYD-2/Liprin- α in
532 *Caenorhabditis elegans*. *J. Neurosci.* 41, 4782–4794.
- 533 Reddy-Alla, S., Bohme, M.A., Reynolds, E., Beis, C., Grasskamp, A.T., Mampell, M.M.,
534 Maglione, M., Jusyte, M., Rey, U., Babikir, H., et al. (2017). Stable Positioning of Unc13
535 Restricts Synaptic Vesicle Fusion to Defined Release Sites to Promote Synchronous
536 Neurotransmission. *Neuron* 95, 1350-1364.e12.
- 537 Richmond, J.E., Davis, W.S., and Jorgensen, E.M. (1999). UNC-13 is required for synaptic
538 vesicle fusion in *C. elegans*. *Nat. Neurosci.* 2, 959–964.
- 539 Rosenmund, C., and Stevens, C.F. (1996). Definition of the readily releasable pool of vesicles at
540 hippocampal synapses. *Neuron* 16, 1197–1207.
- 541 Rosenmund, C., Sigler, A., Augustin, I., Reim, K., Brose, N., and Rhee, J.S. (2002). Differential
542 control of vesicle priming and short-term plasticity by Munc13 isoforms. *Neuron* 33, 411–424.
- 543 Sakamoto, H., Ariyoshi, T., Kimpara, N., Sugao, K., Taiko, I., Takikawa, K., Asanuma, D.,
544 Namiki, S., and Hirose, K. (2018). Synaptic weight set by Munc13-1 supramolecular
545 assemblies. *Nat. Neurosci.* 21, 41–49.
- 546 Sando, R., Bushong, E., Zhu, Y., Huang, M., Considine, C., Phan, S., Ju, S., Uytiepo, M.,
547 Ellisman, M., and Maximov, A. (2017). Assembly of Excitatory Synapses in the Absence of
548 Glutamatergic Neurotransmission. *Neuron* 94, 312-321.e3.
- 549 Sigler, A., Oh, W.C., Imig, C., Altas, B., Kawabe, H., Cooper, B.H., Kwon, H.-B., Rhee, J.-S.,
550 and Brose, N. (2017). Formation and Maintenance of Functional Spines in the Absence of
551 Presynaptic Glutamate Release. *Neuron* 94, 304-311.e4.
- 552 Siksou, L., Varoqueaux, F., Pascual, O., Triller, A., Brose, N., and Marty, S. (2009). A common
553 molecular basis for membrane docking and functional priming of synaptic vesicles. *Eur. J.
554 Neurosci.* 30, 49–56.
- 555 Südhof, T.C. (2012). The Presynaptic Active Zone. *Neuron* 75, 11–25.
- 556 Tan, C., Wang, S.S.H., de Nola, G., and Kaeser, P.S. (2022). Rebuilding essential active zone
557 functions within a synapse. *Neuron* 110, 1498-1515.e8.
- 558 Varoqueaux, F., Sigler, A., Rhee, J.S., Brose, N., Enk, C., Reim, K., and Rosenmund, C. (2002).
559 Total arrest of spontaneous and evoked synaptic transmission but normal synaptogenesis in
560 the absence of Munc13-mediated vesicle priming. *Proc. Natl. Acad. Sci. U. S. A.* 99, 9037–
561 9042.
- 562 Verhage, M., Maia, A.S., Plomp, J.J., Brussaard, a B., Heeroma, J.H., Vermeer, H., Toonen,
563 R.F., Hammer, R.E., van den Berg, T.K., Missler, M., et al. (2000). Synaptic assembly of the
564 brain in the absence of neurotransmitter secretion. *Science* 287, 864–869.

- 565 Wang, S.S.H., Held, R.G., Wong, M.Y., Liu, C., Karakhanyan, A., and Kaeser, P.S. (2016).
566 Fusion Competent Synaptic Vesicles Persist upon Active Zone Disruption and Loss of
567 Vesicle Docking. *Neuron* **91**, 777–791.
- 568 Wojcik, S.M., and Brose, N. (2007). Regulation of membrane fusion in synaptic excitation-
569 secretion coupling: speed and accuracy matter. *Neuron* **55**, 11–24.
- 570 Wong, M.Y., Liu, C., Wang, S.S.H., Roquas, A.C.F., Fowler, S.C., and Kaeser, P.S. (2018).
571 Liprin- α 3 controls vesicle docking and exocytosis at the active zone of hippocampal
572 synapses. *Proc. Natl. Acad. Sci. U. S. A.* **115**, 2234–2239.
- 573 Zarebidaki, F., Camacho, M., Brockmann, M.M., Trimbuch, T., Herman, M.A., and Rosenmund,
574 C. (2020). Disentangling the Roles of RIM and Munc13 in Synaptic Vesicle Localization and
575 Neurotransmission. *J. Neurosci.* **40**, 9372–9385.
- 576 Zucker, R.S., and Regehr, W.G. (2002). Short-term synaptic plasticity. *Annu. Rev. Physiol.* **64**,
577 355–405.
- 578

Materials and Methods

Key Resources Table				
Reagent type (species) or resource	Designation	Source or reference	Identifiers	Additional information
genetic reagent (<i>M. musculus</i>)	<i>Rims1</i> ^{tm3Sud} /J (RIM1αβ ^{f/f})	(Kaeser et al., 2008)	RRID: IMSR_JAX:015832	
genetic reagent (<i>M. musculus</i>)	<i>Rims2</i> ^{tm1.1Sud} /J (RIM2αβγ ^{f/f})	(Kaeser et al., 2011)	RRID: IMSR_JAX:015833	
genetic reagent (<i>M. musculus</i>)	<i>Erc1</i> ^{tm2.1Sud} /J (ELKS1α ^{f/f})	(Liu et al., 2014)	RRID: IMSR_JAX:015830	
genetic reagent (<i>M. musculus</i>)	<i>Erc2</i> ^{tm1.2Sud} /J (ELKS2α ^{f/f})	(Kaeser et al., 2009)	RRID: IMSR_JAX:015831	
genetic reagent (<i>M. musculus</i>)	<i>Unc13a</i> ^{f/f} (Munc13-1 ^{f/f})	(Banerjee et al., 2022)	N/A	
genetic reagent (<i>M. musculus</i>)	<i>Unc13b</i> ^{tm1Rmnd} (Munc13-2 ^{-/-})	(Varoqueaux et al., 2002)	RRID_MGI: 2449706	
genetic reagent (<i>M. musculus</i>)	<i>Unc13c</i> ^{tm1Bros} (Munc13-3 ^{-/-})	(Augustin et al., 2001)	RRID_MGI: 2449467	
cell line (<i>Homo sapiens</i>)	HEK293T cells	ATCC	Cat#: CRL-3216 RRID: CVCL_0063	
recombinant DNA reagent	pFSW EGFP Cre	(Liu et al., 2014)	pHN131014, lab plasmid code (LPC): p009	
recombinant DNA reagent	pFSW EGFP ΔCre	(Liu et al., 2014)	pHN131015, LPC: p010	
antibody	anti-RIM (rabbit polyclonal)	SySy	Cat#: 140 003; RRID: AB_887774, lab antibody code (LAC): A58	Immunofluorescence (IF) (1:500)
antibody	anti-PSD-95 (mouse monoclonal)	NeuroMab	Cat#: 73-028; RRID: AB_10698024, LAC: A149	IF (1:500)
antibody	anti-Synaptophysin (guinea pig polyclonal)	SySy	Cat#: 101 004; RRID: AB_1210382, LAC: A106	IF (1:500)
antibody	anti-Munc13-1 (rabbit polyclonal)	SySy	Cat#: 126 103; RRID: AB_887733, LAC: A72	IF (1:500); Western blot (WB) (1:1000)

antibody	anti-Synapsin (mouse monoclonal)	SySy	Cat#: 106 001; RRID: AB_2617071, LAC: A57	WB (1:4000)
antibody	anti-rabbit Alexa Fluor 488 (goat polyclonal)	Thermo Fisher	Cat#: A-11034; RRID: AB_2576217, LAC: S5	IF (1:200)
antibody	anti-mouse IgG2a Alexa Fluor 555 (goat polyclonal)	Thermo Fisher	Cat#: A-21137; RRID: AB_2535776, LAC: S20	IF (1:200)
antibody	anti-guinea pig Alexa Fluor 633 (goat polyclonal)	Thermo Fisher	Cat#: A-21105; RRID: AB_2535757, LAC: S34	IF (1:500)
antibody	anti-mouse peroxidase-conjugated (goat polyclonal)	MP Biologicals	Cat#: 0855550; RRID: AB_2334540; LAC: S52	WB (1:10000)
antibody	anti-rabbit peroxidase-conjugated (goat polyclonal)	MP Biologicals	Cat#: 0855676; RRID: AB_2334589; LAC: S53	WB (1:10000)
software, algorithm	MATLAB	MathWorks	RRID: SCR_001622; https://www.mathworks.com/products/matlab.html	
software, algorithm	Prism	GraphPad	RRID: SCR_002798; https://www.graphpad.com/scientific-software/prism	
software, algorithm	Fiji/ImageJ	NIH	RRID: SCR_002285; https://imagej.net/software/fiji/downloads	
software, algorithm	pClamp	Molecular Devices	RRID: SCR_011323; https://www.moleculardevices.com/products/software/pclamp.html	
software, algorithm	Custom MATLAB code	(Liu, 2022)	doi.org/10.5281/zenodo.6388196	

581

582 **Mouse lines.** The quadruple homozygote floxed mice for *Rims1* (to remove RIM1 α and RIM1 β ,
 583 RRID: IMSR_JAX:015832, (Kaeser et al., 2008)), *Rims2* (to remove RIM2 α , RIM2 β and RIM2 γ ,
 584 (RRID: IMSR_JAX:015833, (Kaeser et al., 2011)), *Erc1* (to remove ELKS1 α , RRID:
 585 IMSR_JAX:015830, (Liu et al., 2014)) and *Erc2* (to remove ELKS2 α , RRID: IMSR_JAX:015831,

586 (Kaeser et al., 2009)) were previously described (Wang et al., 2016). Exon 6 (E6) or 26 (E26)
587 were flanked by loxP sites in the *Rims1* or *Rims2* floxed mice, respectively. Exons 2 (E2) and 3
588 (E3) were flanked by loxP sites in the *Erc1* floxed mice, and exon 3 (E3) was flanked by loxP
589 sites in the *Erc2* floxed mice. Floxed *Unc13a* (Munc13-1, Exon 21 (E21) flanked by loxP sites)
590 mice (Banerjee et al., 2022) were crossed to constitutive knockout mice for *Unc13b* (Munc13-2,
591 *Unc13b*^{tm1Rmnd}, RRID_MGI:2449706, (Varoqueaux et al., 2002)) and *Unc13c* (Munc13-3,
592 *Unc13c*^{tm1Bros}, RRID_MGI:2449467, (Augustin et al., 2001)) to produce Munc13 triple
593 homozygote mice. Mice for simultaneous ablation of RIM1, RIM2, ELKS1, ELKS2, Munc13-1
594 and Munc13-2 were generated by crossing the corresponding conditional (RIM1 $\alpha\beta$, RIM2 $\alpha\beta\gamma$,
595 ELKS1 α , ELKS2 α , and Munc13-1) and constitutive (Munc13-2) knockout alleles to
596 homozygosity. All animal experiments were approved by the Harvard University Animal Care
597 and Use Committee (protocol number IS00000049).

598

599 **Cell lines, primary neuronal culture, and lentiviral infection.** Primary mouse hippocampal
600 cultures were generated from newborn pups within 24 h after birth as described (Held et al.,
601 2020; Tan et al., 2022; Wang et al., 2016); cells from mice of both sexes were mixed. Mice were
602 anesthetized on ice and the hippocampus was dissected out. Cells were dissociated and plated
603 onto glass coverslips in tissue culture medium composed of Minimum Essential Medium (MEM)
604 with 10% Fetal Select bovine serum (Atlas Biologicals FS-0500-AD), 2 mM L-glutamine, and 25
605 μ g/mL insulin, 0.1 mg/mL transferrin, 0.5% glucose, 0.02% NaHCO₃. Cultures were maintained
606 in a 37 °C-tissue culture incubator, and after ~24 h the plating medium was exchanged with
607 growth medium composed of MEM with 5% Fetal Select bovine serum, 2% B-27 supplement
608 (Thermo Fisher 17504044), 0.5 mM L-glutamine, 0.1 mg/mL transferrin, 0.5% glucose, 0.02%
609 NaHCO₃. At DIV3, depending on growth, 50% or 75% of the medium were exchanged with
610 growth medium supplemented with 4 μ M Cytosine β -D-arabinofuranoside (AraC) to inhibit glial
611 cell growth. Cultured neurons were infected with lentiviruses produced in HEK293T cells (CRL-

612 3216, RRID: CVCL_0063, immortalized cell line of female origin, purchased mycoplasma-free)
613 by Ca²⁺ phosphate transfection at DIV5 unless noted otherwise. These lentiviruses expressed
614 EGFP-tagged Cre recombinase (to generate cKO neurons) or a truncated, enzymatically
615 inactive EGFP-tagged Cre protein (Δ Cre, to generate control neurons). Expression in lentiviral
616 constructs was driven by the human Synapsin promoter to restrict expression to neurons (Liu et
617 al., 2014; Wang et al., 2016). Analyses were performed at DIV16-19.

618

619 **Electrophysiology.** Electrophysiological recordings in cultured hippocampal neurons were
620 performed as described (Held et al., 2020; Tan et al., 2022; Wang et al., 2016) at DIV16-19. The
621 extracellular solution contained (in mM): 140 NaCl, 5 KCl, 2 MgCl₂, 1.5 CaCl₂, 10 glucose, 10
622 HEPES-NaOH (pH 7.4, ~300 mOsm). To avoid network activity induced by AMPA receptor
623 activation, NMDAR-mediated excitatory postsynaptic currents (NMDAR-EPSCs) were measured
624 to assess action potential-triggered excitatory transmission. For NMDAR-EPSCs, 6-Cyano-7-
625 nitroquinoxaline-2,3-dione (CNQX, 20 μ M) and picrotoxin (PTX, 50 μ M) were present in the
626 extracellular solution. Inhibitory postsynaptic currents (IPSCs) were recorded in the presence of
627 D-amino-5-phosphonopentanoic acid (D-APV, 50 μ M) and CNQX (20 μ M) in the extracellular
628 solution. Recordings were performed at room temperature (20 - 24 °C). Action potentials were
629 elicited with a bipolar focal stimulation electrode fabricated from nichrome wire. Paired pulse
630 ratios were calculated as the amplitude of the second PSC divided by the amplitude of the first
631 at each interval from the average of 6 sweeps per cell and interval. The baseline value for the
632 second PSC was taken immediately after the second stimulus artifact. For analysis of action
633 potential trains (50 stimuli at 10 Hz), the baseline value of each IPSC within the train was taken
634 immediately after the corresponding stimulus artifact. For AMPAR-mediated mEPSC and
635 sucrose-induced EPSC recordings, TTX (1 μ M), PTX (50 μ M), and D-APV (50 μ M) were added
636 to the extracellular solution. For mIPSC and sucrose-induced IPSC recordings, TTX (1 μ M),
637 CNQX (20 μ M), and D-APV (50 μ M) were added to the extracellular solution. The RRP was

estimated by application of 500 mM sucrose in extracellular solution applied via a microinjector syringe pump for 10 s at a rate of 10 μ l/min through a tip with an inner diameter of 250 μ m. mEPSCs and mIPSCs were identified with a template search followed by manual confirmation by an experimenter, and their frequencies and amplitudes were assessed during a 100-s recording time window after reaching a stable baseline (> 3 min after break-in). Glass pipettes were pulled at 2 - 5 M Ω and filled with intracellular solutions containing (in mM) for EPSC recordings: 120 Cs-methanesulfonate, 2 MgCl₂, 10 EGTA, 4 Na₂-ATP, 1 Na-GTP, 4 QX314-Cl, 10 HEPES-CsOH (pH 7.4, ~300 mOsm) and for IPSC recordings: 40 CsCl, 90 K-gluconate, 1.8 NaCl, 1.7 MgCl₂, 3.5 KCl, 0.05 EGTA, 2 Mg-ATP, 0.4 Na₂-GTP, 10 phosphocreatine, 4 QX314-Cl, 10 HEPES-CsOH (pH 7.2, ~300 mOsm). Cells were held at +40 mV for NMDAR-EPSC recordings and at -70 mV for evoked IPSC, mEPSC, mIPSC, sucrose EPSC and sucrose IPSC recordings. Access resistance was monitored and compensated to 3-5 M Ω , and cells were discarded if the uncompensated access exceeded 15 M Ω . Data were acquired at 5 kHz and lowpass filtered at 2 kHz with an Axon 700B Multiclamp amplifier and digitized with a Digidata 1440A digitizer. Data acquisition and analyses were done using pClamp10. For electrophysiological experiments, the experimenter was blind to the genotype throughout data acquisition and analyses.

STED and confocal imaging. Light microscopic analyses were in essence performed as previously described (Emperador-Melero et al., 2021b, 2021a; Held et al., 2020; Tan et al., 2022; Wong et al., 2018). Neurons were cultured on 0.17 mm thick 12 mm diameter coverslips. At DIV16-18, cultured neurons were washed two times with warm PBS, and fixed in 4% PFA in PBS for 10 min. After fixation, coverslips were rinsed twice in PBS, then permeabilized in PBS + 0.1% Triton X-100 + 3% BSA (TBP) for 1 h. Primary antibodies were diluted in TBP and stained for 24-48 h at 4 °C. The following primary antibodies were used: rabbit anti-RIM1 (1:500, RRID: AB_887774, A58), rabbit anti-Munc13-1 (1:500, RRID: AB_887733, A72), guinea pig anti-

664 Synaptophysin (1:500, RRID: AB_1210382, A106), mouse anti-PSD-95 (1:500, RRID:
665 AB_10698024, A149). After primary antibody staining, coverslips were rinsed twice and washed
666 3-4 times for 5 min in TBP. Alexa Fluor 488 (anti-rabbit, RRID: AB_2576217, S5), 555 (anti-
667 mouse IgG2a, RRID: AB_1500824, S20), and 633 (anti-guinea pig, RRID: AB_2535757, S34)
668 conjugated antibodies were used as secondary antibodies at 1:200 (Alexa Fluor 488 and 555)
669 or 1:500 (Alexa Fluor 633) dilution in TBP, incubated for 24-48 h at 4 °C followed by rinsing two
670 times and washing 3-4 times 5 min in TBP. Stained coverslips were post-fixed for 10 min with 4%
671 PFA in PBS, rinsed two times in PBS + 50 mM glycine and once in deionized water, air-dried,
672 and mounted on glass slides. STED images were acquired with a Leica SP8 Confocal/STED 3X
673 microscope with an oil immersion 100x 1.44 numerical aperture objective and gated detectors
674 as described before (Emperador-Melero et al., 2021a; Held et al., 2020; Tan et al., 2022; Wong
675 et al., 2018). Images of 46.51 x 46.51 μm^2 areas were scanned at a pixel density of 4096 x 4096
676 (11.358 nm/pixel). Alexa Fluor 633, Alexa Fluor 555, and Alexa Fluor 488 were excited with 633
677 nm, 555 nm and 488 nm using a white light laser at 2-5% of 1.5 mW laser power. The Alexa
678 Fluor 633 channel was acquired first in confocal mode using 2x frame averaging. Subsequently,
679 Alexa Fluor 555 and Alexa Fluor 488 channels were acquired in both confocal and STED modes.
680 Alexa Fluor 555 and 488 channels in STED mode were depleted with 660 nm (50% of max
681 power, 30% axial depletion) and 592 nm (80% of max power, 30% axial depletion) depletion
682 lasers, respectively. Line accumulation (2-10x) and frame averaging (2x) were applied during
683 STED scanning. Identical settings were applied to all samples within an experiment. Synapses
684 within STED images were selected in side-view, defined as synapses that contained a synaptic
685 vesicle cluster labeled with Synaptophysin and associated with an elongated PSD-95 structure
686 along the edge of the vesicle cluster as described (Emperador-Melero et al., 2021b, 2021a;
687 Held et al., 2020; de Jong et al., 2018; Nyitrai et al., 2020; Tan et al., 2022; Wong et al., 2018).
688 For intensity profile analyses, side-view synapses were selected using only the PSD-95 signal
689 and the vesicle signal for all experiments by an experimenter blind to the protein of interest. A

region of interest (ROI) was manually drawn around the PSD-95 signal and fit with an ellipse to determine the center position and orientation. A ~1200 nm long, 200 nm wide rectangle was then positioned perpendicular to and across the center of the elongated PSD-95 structure. Intensity profiles from -400 nm (presynaptic) to +200 nm (postsynaptic) relative to the center of the PSD-95 signal were obtained for all three channels within this ROI. To align individual profiles, the PSD-95 signal only was smoothed using a moving average of 5 pixels, and the smoothed signal was used to define the peak position of PSD-95. All three channels (vesicle marker, test protein, and smoothed PSD-95) were then aligned to the PSD-95 peak position and averaged across images for line profile plots. Peak values for each line profile were determined independent of peak position and used to generate the plots of peak levels. For Fig. 1 – figure supplements 3A, 3B, 3D, 3F and Fig. 2 – figure supplements 1C, 1D, Munc13-1 levels were analyzed using Synaptophysin to define ROIs in the confocal images with Image J. For Figs. 2L-2O and Fig. 2 – figure supplements 2A-2E, ROI selection was performed using a previously described custom-written code to perform automatic two-dimensional segmentation (Emperador-Melero et al., 2021a; Held et al., 2020; Liu et al., 2018, 2022); the code was deposited to Zenodo at <https://doi.org/10.5281/zenodo.6388196> (Liu, 2022). After Synaptophysin object detection, the density, intensity and area of these objects were quantified (Figs. 2L-2O, Fig. 2 – figure supplements 2A-2D). In Fig. 2 – figure supplement 2E, the Synaptophysin objects (confocal) that exceeded the overlap threshold of 0% with PSD-95 objects (STED) were included in the quantification. Analyses were performed on raw images without background subtraction, and adjustments were done identically across experimental conditions. Representative images were brightness and contrast adjusted to facilitate inspection, and these adjustments were made identically for images within an experiment. The experimenter was blind to the condition/genotype for image acquisition and analyses.

714

715 **High-pressure freezing and electron microscopy.** Neurons were cultured on 6 mm sapphire

716 coverslips coated with matrigel. At DIV16-18, cultured neurons were frozen using a Leica EM
717 ICE high-pressure freezer in extracellular solution containing (in mM): 140 NaCl, 5 KCl, 2 CaCl₂,
718 2 MgCl₂, 10 HEPES-NaOH (pH 7.4), 10 Glucose (~300 mOsm) with PTX (50 µM), CNQX (20
719 µM) and D-AP5 (50 µM) added to block synaptic transmission. After freezing, samples were first
720 freeze-substituted (AFS2, Leica) in anhydrous acetone containing 1% glutaraldehyde, 1%
721 osmium tetroxide, 1% water. The process of freeze substitution was as follows: -90 °C for 5 h,
722 5 °C per h to -20 °C, -20 °C for 12 h, and 10 °C per h to 20 °C. Following freeze substitution,
723 samples were Epon infiltrated, and baked for 48 h at 60 °C followed by 80 °C overnight before
724 sectioning at 50 nm. For ultrathin sectioning, the sapphire coverslip was removed from the resin
725 block by plunging the sample first in liquid nitrogen and followed by warm water several times
726 until the sapphire was completely detached. The resin block containing the neurons was then
727 divided into four pieces, and one piece each was mounted for sectioning. Ultrathin sectioning
728 was performed on a Leica EM UC7 ultramicrotome, and the 50 nm sections were collected on a
729 nickel slot grid (2 x 1 mm) with a carbon coated formvar support film. The samples were
730 counterstained by incubating the grids with 2% lead acetate solution for 10 s, followed by rinsing
731 with distilled water. Images were taken with a transmission electron microscope (JEOL 1200 EX
732 at 80 kV accelerating voltage) and processed with ImageJ. The total number of vesicles, the
733 number of docked vesicles per synapse profile, the area of the presynaptic bouton, and the
734 length of the PSD were analyzed in each section using a custom-written Matlab code (Liu,
735 2022). Docked vesicles were defined as vesicles for which the electron densities of the vesicular
736 membrane and the presynaptic plasma membrane merged such that the two membranes were
737 not separated by less electron dense space. Bouton size was calculated from the measured
738 perimeter of each synapse. Experiments and analyses were performed by an experimenter
739 blind to the genotype.

740

741 **Western blotting.** At DIV15-19, cultured neurons were harvested in 20 µl 1x SDS buffer per

742 coverslip and run on standard SDS-Page gels followed by transfer to nitrocellulose membranes.
743 Membranes were blocked in filtered 10% nonfat milk/5% goat serum for 1 h at room
744 temperature and incubated with primary antibodies (rabbit anti-Munc13-1, 1:1000, RRID:
745 AB_887733, A72; mouse anti-Synapsin, 1:4000, RRID: AB_2617071, A57) in 5% nonfat
746 milk/2.5% goat serum overnight at 4 °C, and HRP-conjugated secondary antibodies (1:10,000,
747 anti-mouse, RRID: AB_2334540; anti-rabbit, RRID: AB_2334589) were used. Western blotting
748 was repeated 3-8 times per genotype from selected cultures used for electrophysiology,
749 immuno staining and electron microscopy. For illustration in figures, images were adjusted for
750 brightness and contrast to facilitate visual inspection, and the same adjustments were used for
751 the entire scan.

752

753 **Statistics.** Statistics were performed in GraphPad Prism 9. Data are displayed as mean ± SEM,
754 and significance is presented as * $P < 0.05$, ** $P < 0.01$, and *** $P < 0.001$. Sample sizes were
755 determined based on previous studies, and no statistical methods were used to predetermine
756 sample size. No outliers were excluded. Parametric tests were used for normally distributed
757 data (assessed by Shapiro-Wilk tests) or when sample size was $n \geq 30$. Unpaired two-tailed
758 Student's t-tests were used for datasets with equal variance, or Welch's unequal variances t-
759 tests for datasets with unequal variance. For non-normally distributed data, Mann-Whitney tests
760 or Kruskal-Wallis test followed by Dunn's multiple comparisons post hoc tests were used. For
761 paired pulse ratios, two-way ANOVA with Bonferroni's post hoc tests was used. For STED side-
762 view analyses, two-way ANOVA with Bonferroni's post hoc tests was used on a 200 nm-window
763 centered around the active zone peak. For all datasets, sample sizes and the specific tests used
764 are stated in the figure legends.

765

766 **Materials, data and code availability.** Plasmids used for this study will be shared without
767 restrictions. Mouse lines will be shared upon request within the limits of the respective material

768 transfer agreements. The previously used code has been deposited to Zenodo and is publicly
769 available as listed in the key resources table. All data generated or analyzed in this study,
770 including individual data points, are included in the figures. Source data files for Fig. 1 – figure
771 supplement 3, Fig. 2 – figure supplement 1 and Fig. 2 – figure supplement 2 are provided, and a
772 source data table that contains all means, errors, statistical tests and p-values is also included.
773 Plasmids and mice should be requested from the corresponding author
774 (kaeser@hms.harvard.edu).

775

776 **Figure legends**

777

778 **Figure 1. Action potential-evoked neurotransmitter release and Munc13 active zone
779 levels after ablation of RIM+ELKS.**

780 **(A)** Targeting strategy for deletion of RIM1, RIM2, ELKS1 and ELKS2 in cultured hippocampal
781 neurons. Neurons of mice with floxed alleles for all four genes were infected with Cre-
782 expressing lentiviruses (to generate cKO^{R+E} neurons) or lentiviruses expressing a
783 recombination-deficient version of Cre (to generate control^{R+E} neurons) as described (Tan et al.,
784 2022; Wang et al., 2016).

785 **(B, C)** Sample traces (B) and quantification (C) of EPSCs evoked by focal electrical stimulation,
786 control^{R+E} 20 cells/3 cultures, cKO^{R+E} 19/3.

787 **(D-F)** Sample traces (D) and quantification of amplitudes (E) and 20-80% rise times (F) of
788 IPSCs evoked by focal electrical stimulation, 18/3 each.

789 **(G-K)** Sample STED images (G) and quantification (H-K) of side-view synapses in cultured
790 hippocampal neurons stained for Munc13-1 (imaged in STED), PSD-95 (imaged in STED), and
791 Synaptophysin (imaged in confocal). In H and I, fluorescence levels at each position of line
792 profiles (600 nm x 200 nm) positioned perpendicular to the center of elongated PSD-95
793 structure and aligned to the PSD-95 peak are shown. In J and K, peak values for each line
794 profile are shown independent of peak position, 60 synapses/3 cultures each.

795 Data are mean ± SEM; *** $P < 0.001$ as determined by Welch's t-tests (C, E and F), two-way
796 ANOVA followed by Bonferroni's multiple comparisons post-hoc tests (H and I), or unpaired two-
797 tailed Student's t-tests (J and K). For assessment of Munc13-1 levels after Munc13 knockout
798 using STED microscopy, Synaptophysin levels in cKO^{R+E} synapses, and comparison of
799 Munc13-1 levels by STED microscopy in cKO^{R+E} and cKO^M synapses, see Fig. 1 – figure
800 supplement 1; for assessment of synaptic transmission after Munc13 knockout, see Fig. 1 –
801 figure supplement 2; for assessment of Munc13-1 expression by confocal microscopy and

802 Western blotting in cKO^{R+E} and cKO^M neurons, see Fig. 1 – figure supplement 3. Source data
803 table 1 contains numerical values of all means, errors, and p-values for this and all following
804 figures.

805

806 **Figure 2. Simultaneous deletion of RIM, ELKS and Munc13 does not disrupt synapse**
807 **formation.**

808 **(A)** Targeting strategy for simultaneous deletion of RIM1, RIM2, ELKS1, ELKS2, Munc13-1 and
809 Munc13-2 in cultured hippocampal neurons (cKO^{R+E+M}). Neurons were infected with Cre-
810 expressing lentiviruses (to generate cKO^{R+E+M} neurons) or viruses expressing a recombination-
811 deficient version of Cre (to generate control^{R+E+M} neurons).

812 **(B-F)** Sample STED images (B) and quantification (C-F) of side-view synapses stained for RIM1
813 (STED), PSD-95 (STED) and Synaptophysin (confocal), control^{R+E+M} 65 synapses/3 cultures,
814 cKO^{R+E+M} 66/3.

815 **(G-K)** Same as B-F, but for synapses stained for Munc13-1 instead of RIM1, 63/3 each.

816 **(L-O)** Overview confocal images of anti-Synaptophysin staining (L) and quantification of
817 Synaptophysin puncta density (M), intensity (N) and size (O); Synaptophysin objects were
818 detected using automatic two-dimensional segmentation, confocal images of Synaptophysin
819 staining are from the experiment shown in B-F, 17 images/3 cultures each.

820 Data are mean ± SEM; ***P < 0.001 as determined by two-way ANOVA followed by Bonferroni's
821 multiple comparisons post-hoc tests (C, D, H and I), unpaired two-tailed Student's t-tests (E, J,
822 M-O), or Welch's t-tests (F and K). For Synaptophysin levels in cKO^{R+E+M} synapses, comparison
823 of Munc13-1 levels by STED microscopy in cKO^{R+E} and cKO^{R+E+M} neurons, and Munc13-1
824 expression in control^{R+E+M} and cKO^{R+E+M} neurons assessed by confocal microscopy and
825 Western blotting, see Fig. 2 – figure supplement 1; for microscopic assessment of synapse
826 formation after lentiviral infection at DIV2 instead of DIV5, see Fig. 2 – figure supplement 2.

827

828 **Figure 3. Synaptic ultrastructure after RIM+ELKS+Munc13 knockout.**

829 **(A-E)** Sample images (A) and analyses (B-E) of synaptic morphology of high-pressure frozen
830 neurons analyzed by electron microscopy; docked vesicles (B), total vesicles (C), bouton size
831 (D) and PSD length (E) per synapse profile are shown. Docked vesicles were defined as
832 vesicles for which the electron densities of the vesicular and target membranes merge such that
833 they are not separated by less electron dense space, control^{R+E+M} 99 synapses/2 cultures,
834 cKO^{R+E+M} 100/2.

835 Data are mean ± SEM; *P < 0.05, ***P < 0.001 as determined by Welch's t-tests (B and C), or
836 by unpaired t two-tailed Student's tests (D and E).

837

838 **Figure 4. Neurotransmitter release is strongly impaired after RIM+ELKS+Munc13 ablation.**

839 **(A-C)** Sample traces (A) and quantification of mEPSC frequencies (B) and amplitudes (C) in
840 control^{R+E+M} and cKO^{R+E+M} neurons, 27 cells/3 cultures each.

841 **(D-F)** Sample traces (D) and quantification of mIPSC frequencies (E) and amplitudes (F), 22/3
842 each.

843 **(G, H)** Sample traces (G) and quantification (H) of EPSCs evoked by focal electrical stimulation,
844 20/3 each.

845 **(I-K)** Sample traces (I) and quantification of amplitudes (J) and 20-80% rise times (K) of IPSCs
846 evoked by focal electrical stimulation, control^{R+E+M} 28/3, cKO^{R+E+M} 31/3.

847 **(L)** Comparison of EPSCs normalized to their own controls for cKO^{R+E} (absolute data from Fig.
848 1C) and cKO^{R+E+M} (from H) neurons, cKO^{R+E} 19/3, cKO^{R+E+M} 20/3.

849 **(M)** Comparison of IPSCs normalized to their own controls for cKO^{R+E} (absolute data from Fig.
850 1E) and cKO^{R+E+M} (from J) neurons, cKO^{R+E} 18/3, cKO^{R+E+M} 31/3.

851 Data are mean ± SEM; **P < 0.01, ***P < 0.001 as determined by Welch's t-tests (K and L), or
852 Mann-Whitney tests (B, C, E, F, H, J and M). For mEPSC and mIPSC kinetics in cKO^{R+E+M}
853 neurons, see Fig. 4 – figure supplement 1.

854

855 **Figure 5. The remaining functional RRP in RIM+ELKS-deficient synapses depends on**
856 **Munc13.**

857 **(A, B)** Sample traces (A) and quantification (B) of EPSCs triggered by hypertonic sucrose in
858 control^{R+E} and cKO^{R+E} neurons, the first 10 s of the EPSC were quantified to estimate the RRP,
859 control^{R+E} 18 cells/3 cultures, cKO^{R+E} 17/3.

860 **(C, D)** As A and B, but for IPSCs, 18/3 each.

861 **(E-H)** As for A-D, but for control^{R+E+M} and cKO^{R+E+M} neurons, F: 23/3 each, H: 21/3 each.

862 **(I)** Comparison of EPSCs triggered by hypertonic sucrose normalized to their own controls for
863 cKO^{R+E} (absolute data from B) and cKO^{R+E+M} (from F), cKO^{R+E} 17/3, cKO^{R+E+M} 23/3.

864 **(J)** Comparison of IPSCs triggered by hypertonic sucrose normalized to their own controls for
865 cKO^{R+E} (absolute data from D) and cKO^{R+E+M} (from H), cKO^{R+E} 18/3, cKO^{R+E+M} 21/3.

866 Data are mean ± SEM; ** $P < 0.01$, *** $P < 0.001$ as determined by Mann-Whitney tests (B, F, H,
867 I and J) or Welch's t-tests (D).

868

869 **Figure 6. Vesicular release probability is not further impaired by combined**
870 **RIM+ELKS+Munc13 knockout.**

871 **(A, B)** Sample traces (A) and quantification (B) of EPSC paired pulse ratios in control^{R+E} and
872 cKO^{R+E} neurons, control^{R+E} 15 cells/3 cultures, cKO^{R+E}, 16/3.

873 **(C, D)** As A and B, but for IPSCs (sample traces of 2500-ms intervals are not shown in C for
874 simplicity), 17/3 each.

875 **(E-H)** As for A-D, but for control^{R+E+M} and cKO^{R+E+M} neurons, F: 19/3 each, H: 19/3 each.

876 **(I)** Comparison of EPSC paired pulse ratios across interstimulus intervals normalized to their
877 own controls for cKO^{R+E} (absolute data from B) and cKO^{R+E+M} (from F), cKO^{R+E} 16/3, cKO^{R+E+M}
878 19/3.

879 **(J)** Comparison of IPSC paired pulse ratios across interstimulus intervals normalized to their

880 own controls for cKO^{R+E} (absolute data from D) and cKO^{R+E+M} (from H), cKO^{R+E} 17/3, cKO^{R+E+M}
881 19/3.

882 Data are mean \pm SEM; *** $P < 0.001$ as determined by two-way ANOVA followed by Bonferroni's
883 multiple comparisons post-hoc tests (B, D, F and H), or by Mann-Whitney tests (I and J). For
884 mEPSCs and mIPSCs in cKO^{R+E} neurons, and for IPSCs evoked by stimulus trains in cKO^{R+E}
885 and cKO^{R+E+M} neurons, see Fig. 6 – figure supplement 1.

886

887 **Figure 1 – figure supplement 1. Assessment of Munc13-1 levels with STED microscopy in**
888 **Munc13 knockout synapses.**

889 **(A)** Targeting strategy for deletion of Munc13-1, Munc13-2 and Munc13-3 in cultured
890 hippocampal neurons (cKO^M). Cultured hippocampal neurons of mice with floxed alleles for
891 Munc13-1 (Banerjee et al., 2022) and constitutive knockout alleles for Munc13-2 (Varoqueaux et
892 al., 2002) and Munc13-3 (Augustin et al., 2001) were infected with Cre-expressing lentiviruses
893 (to generate cKO^M neurons) or with lentiviruses expressing a recombination-deficient Cre (to
894 generate control^M neurons).

895 **(B-F)** Sample STED images (B) and quantification (C-F) of side-view synapses in cultured
896 hippocampal neurons stained for Munc13-1 (STED), PSD-95 (STED), and Synaptophysin
897 (confocal), 60 synapses/3 cultures each.

898 **(G)** Comparison of Munc13-1 levels normalized to their own controls in cKO^{R+E} (absolute data
899 from Fig. 1I) and cKO^M (from D) synapses, 60 synapses/3 cultures each. The red line is the
900 calculated ratio of normalized Munc13-1 levels from cKO^{R+E} to cKO^M.

901 **(H)** Quantification of Synaptophysin levels in side-view synapses of control^M and cKO^M neurons
902 for the experiment shown in B-D, 60 synapses/3 cultures each.

903 **(I)** Same as H, but for Synaptophysin levels in control^{R+E} and cKO^{R+E} neurons for the experiment
904 shown in Figs. 1G-1I, 60 synapses/3 cultures each.

905 Data are mean \pm SEM; *** $P < 0.001$ as determined by two-way ANOVA followed by Bonferroni's

906 multiple comparisons post-hoc tests (C, D and G-I; in G, ratios were not used for statistics),
907 unpaired two-tailed Student's t-tests (E), or Welch's t-test (F).

908

909 **Figure 1 – figure supplement 2. Action potential-evoked neurotransmitter release after
910 ablation of Munc13.**

911 (A, B) Sample traces (A) and quantification (B) of EPSCs evoked by focal electrical stimulation
912 in control^M and cKO^M neurons, 16 cells/3 cultures each.

913 (C-E) Sample traces (C) and quantification of amplitudes (D) and 20-80% rise times (E) of
914 IPSCs evoked by focal electrical stimulation, 26/3 each.

915 Data are mean ± SEM; ***P < 0.001 as determined by Mann-Whitney tests (B, D and E).

916

917 **Figure 1 – figure supplement 3. Assessment of Munc13-1 levels with confocal
918 microscopy and Western blot in RIM+ELKS or Munc13 knockout neurons.**

919 (A, B) Sample confocal images (A) and quantification of Munc13-1 levels (B) at synapses of
920 control^{R+E} and cKO^{R+E} neurons. Confocal microscopic images were taken from the same set of
921 cultures that were analyzed by STED in Fig. 1. Synaptophysin staining was used to define ROIs,
922 and levels of Munc13-1 were quantified within those ROIs, control^{R+E} 16 images/3 cultures,
923 cKO^{R+E}, 19/3.

924 (C) Western blot of homogenates of cultured control^{R+E} and cKO^{R+E} neurons using anti-Munc13-
925 1 antibodies and anti-Synapsin antibodies as loading controls. Representative examples of 6
926 cultures assessed by Western blotting are shown.

927 (D, E) As in A and B, but for cKO^M neurons, control^M 16/3, cKO^M, 17/3.

928 (F) As in C, but for control^M and cKO^M neurons, the results shown here are from exposures to
929 film that lasted ≤ 1 min. The very low levels of an alternative variant of Munc13-1 left in Munc13-
930 1 knockout neurons generated from this allele, as described in Fig. S2 of (Banerjee et al., 2022),
931 is not detected in these short exposures. Representative examples of 6 cultures assessed by

932 Western blotting are shown.
933 Data are mean \pm SEM; *** $P < 0.001$ as determined by Mann-Whitney tests (B) or Welch's t-test
934 (E). For source data of C and F, see Fig. 1 – figure supplement 3 – source data 1.

935

936 **Figure 2 – figure supplement 1. Assessment of Munc13-1 levels in RIM+ELKS+Munc13**
937 **knockout neurons.**

938 (A) Quantification of Synaptophysin distribution aligned to the PSD-95 peak in side-view
939 synapses of cultured control^{R+E+M} and cKO^{R+E+M} neurons from the experiment shown in Figs. 2B-
940 2D, control^{R+E+M} 65 synapses/3 cultures, cKO^{R+E+M} 66/3.
941 (B) Comparison of Munc13-1 levels normalized to their own controls in cKO^{R+E} (absolute data
942 from Fig. 1I, normalized data replotted from Fig. 1 – figure supplement 1G) and cKO^{R+E+M}
943 (absolute data from Fig. 2I) synapses, cKO^{R+E} 60 synapses/3 cultures, cKO^{R+E+M} 63/3. The
944 green line is the calculated ratio of normalized Munc13-1 levels from cKO^{R+E} to cKO^{R+E+M}.
945 (C, D) Sample confocal images (C) and quantification (D) of Munc13-1 levels at control^{R+E+M} and
946 cKO^{R+E+M} synapses. Synaptophysin staining was used to define regions of interest (ROIs), and
947 levels of Munc13-1 were quantified within those ROIs, 15 images/3 cultures each.
948 (E) Comparison of Munc13-1 levels normalized to their own controls for cKO^{R+E} (absolute data
949 from Fig. 1 – figure supplement 3B), cKO^M (from Fig. 1 – figure supplement 3E) and cKO^{R+E+M}
950 (from D), cKO^{R+E} 19/3, cKO^M 17/3, cKO^{R+E+M} 15/3.
951 (F) Western blot of homogenates of cultured control^{R+E+M} and cKO^{R+E+M} neurons using anti-
952 Munc13-1 antibodies and anti-Synapsin antibodies as loading controls. Representative
953 examples of 8 cultures assessed by Western blotting are shown.
954 Data are mean \pm SEM; ** $P < 0.01$, *** $P < 0.001$ as determined by two-way ANOVA followed by
955 Bonferroni's multiple comparisons post-hoc tests (A and B; in B, ratios were not used for
956 statistics), Welch's t-tests (D), or Kruskal-Wallis tests followed by Dunn's multiple comparisons
957 post hoc tests (E). For source data of F, see Fig. 2 – figure supplement 1 – source data 1.

958

959 **Figure 2 – figure supplement 2. Assessment of Synaptophysin fluorescence in**
960 **RIM+ELKS+Munc13 knockout neurons after lentiviral infection at DIV2.**

961 (A-E) Overview images of anti-Synaptophysin (confocal) and anti-PSD-95 (STED) staining (A)
962 and quantification of Synaptophysin puncta density (B), intensity (C), size (D), and of the density
963 of puncta that contain both Synaptophysin and PSD-95 (E), from cultured control^{R+E+M} and
964 cKO^{R+E+M} neurons infected with lentiviruses (expressing cre recombinase or a recombination-
965 deficient version of Cre) at DIV2 instead of DIV5. Synaptophysin and PSD-95 objects were
966 detected using automatic two-dimensional segmentation, 32 images/3 cultures each.
967 (F) Western blot of homogenates of cultured control^{R+E+M} and cKO^{R+E+M} neurons (infected with
968 lentiviruses at DIV2) using anti-Munc13-1 antibodies and anti-Synapsin antibodies as loading
969 controls. Representative examples of 3 cultures assessed by Western blotting are shown. Data
970 are mean ± SEM; unpaired two-tailed Student's t-tests (B-E) were used. For source data of F,
971 see Fig. 2 – figure supplement 2 – source data 1.

972

973 **Figure 4 – figure supplement 1. Assessment for the kinetics of spontaneous vesicle**
974 **release in RIM+ELKS+Munc13 knockout neurons.**

975 (A) Sample traces of the average mEPSC of a single control^{R+E+M} or cKO^{R+E+M} neuron.
976 (B, C) Quantification of mEPSC rise times (B, 20%-80%) and decay times (C, τ), 27 cells/3
977 cultures each.
978 (D-F) Same as A-C, but for mIPSCs, 22 cells/3 cultures each.
979 Data are mean ± SEM; ***P < 0.001 as determined by Mann-Whitney tests (B, C and E) or
980 unpaired two-tailed Student's t-tests (F).

981

982 **Figure 6 – figure supplement 1. Additional analyses of spontaneous vesicle release and**
983 **IPSCs evoked by stimulus trains in RIM+ELKS and RIM+ELKS+Munc13 knockout**

984 **neurons.**

985 **(A-C)** Sample traces (A) and quantification of mEPSC frequencies (B) and amplitudes (C) in
986 control^{R+E} and cKO^{R+E} neurons, control^{R+E} 21 cells/3 cultures, cKO^{R+E} 23/3.

987 **(D)** Comparison of mEPSC frequencies normalized to their own controls for cKO^{R+E} (absolute
988 data from B) and cKO^{R+E+M} (from Fig. 4B), cKO^{R+E} 23/3, cKO^{R+E+M} 27/3.

989 **(E-G)** Same as A-C, but for mIPSCs, 24/3 each.

990 **(H)** Same as D, but for comparison of mIPSC frequencies for cKO^{R+E} (absolute data from F) and
991 cKO^{R+E+M} (from Fig. 4E), cKO^{R+E} 24/3, cKO^{R+E+M} 22/3.

992 **(I, J)** Sample traces (I) and quantification (J) of IPSC amplitudes evoked by stimulus trains (50
993 stimuli at 10 Hz) in control^{R+E} and cKO^{R+E} neurons, 18/5 each.

994 **(K, L)** Same as I and J, but for control^{R+E+M} and cKO^{R+E+M} neurons, control^{R+E+M} 21/3, cKO^{R+E+M}
995 24/3.

996 Data are mean ± SEM; ***P < 0.001 as determined by Mann-Whitney tests (B-D and F-H) or
997 two-way ANOVA followed by Bonferroni's multiple comparisons post-hoc tests (J and L).

998

999 **Figure 1 – figure supplement 3 – source data 1. Raw scans of Western blots for Figure 1 –**

1000 **figure supplement 3.**

1001 **(A)** Unedited greyscale scans (left) and brightness and contrast adjusted scans (right) of
1002 Western blots shown in Fig. 1 – figure supplement 3C.

1003 **(B)** Same as A, but for Fig. 1 – figure supplement 3F.

1004

1005 **Figure 2 – figure supplement 1 – source data 1. Raw scans of Western blots for Figure 2 –**

1006 **figure supplement 1.**

1007 Unedited greyscale scans (left) and brightness and contrast adjusted scans (right) of Western
1008 blots shown in Fig. 2 – figure supplement 1F.

1009

1010 **Figure 2 – figure supplement 2 – source data 1. Raw scans of Western blots for Figure 2 –**
1011 **figure supplement 2.**

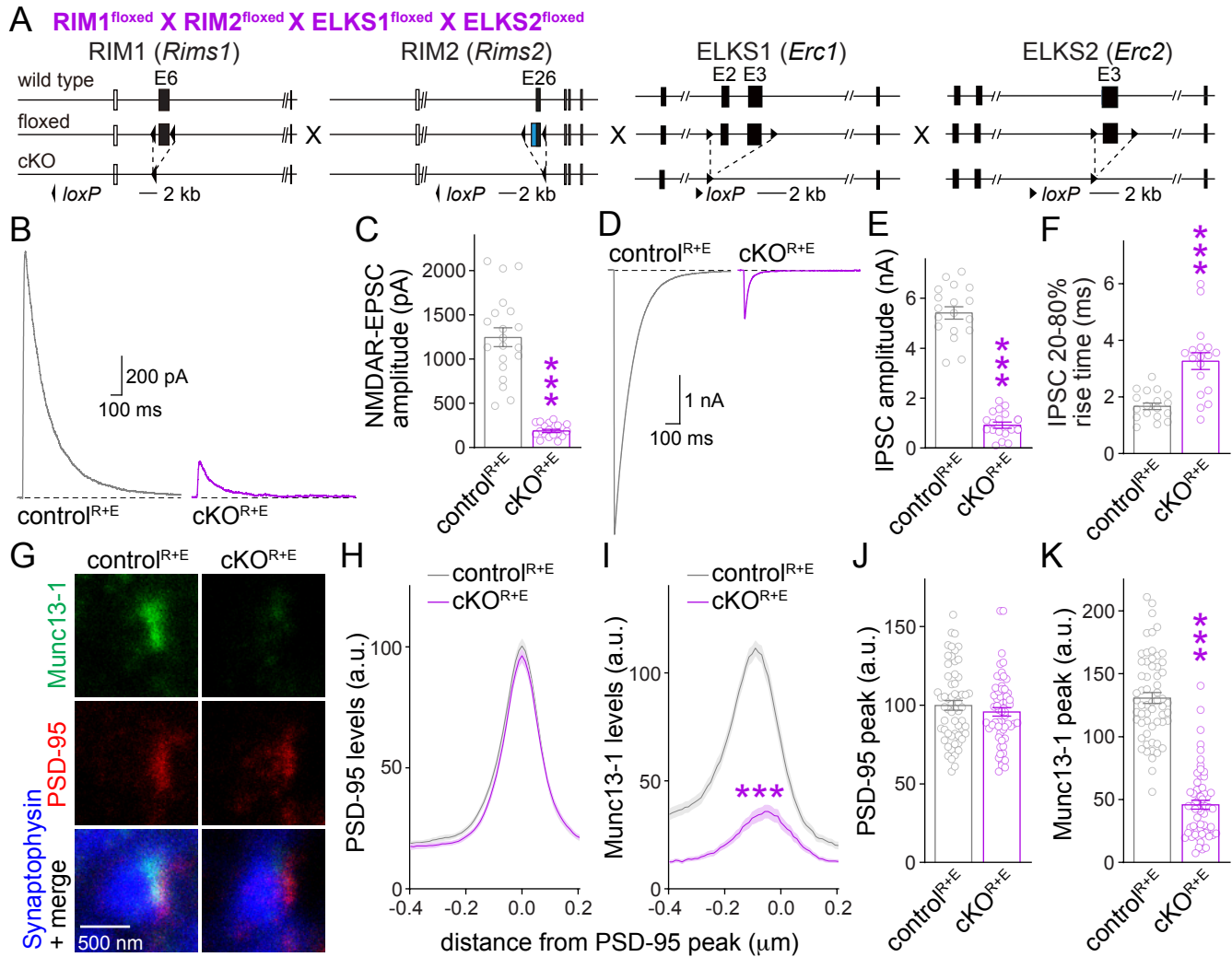
1012 Unedited greyscale scans (left) and brightness and contrast adjusted scans (right) of Western
1013 blots shown in Fig. 2 – figure supplement 2F.

1014

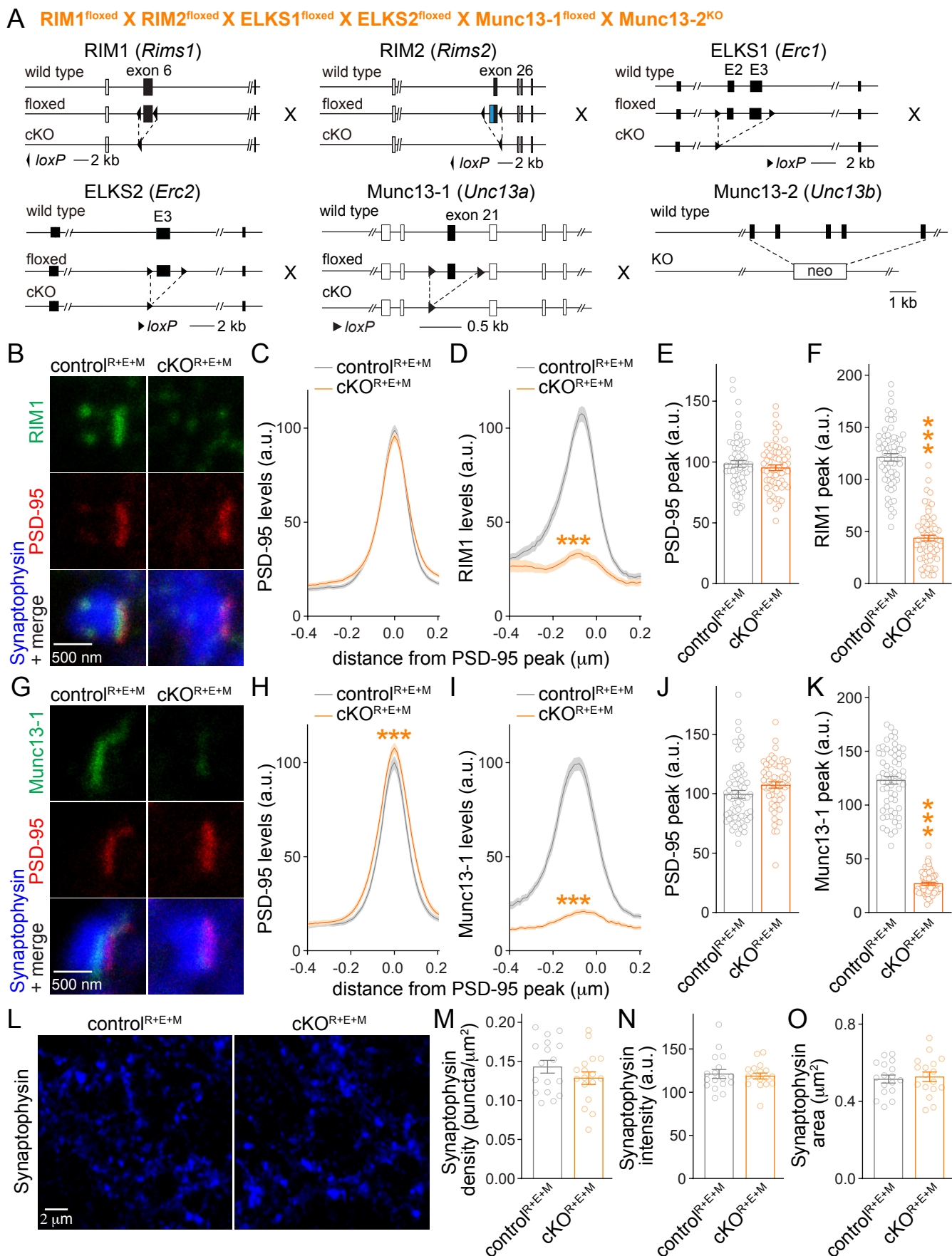
1015 **Source data table 1. Numerical data for all analyses shown in the figures.**

1016 Means, SEMs, statistical tests and p-values for each panel in Figs. 1 to 6 and in corresponding
1017 figure supplements.

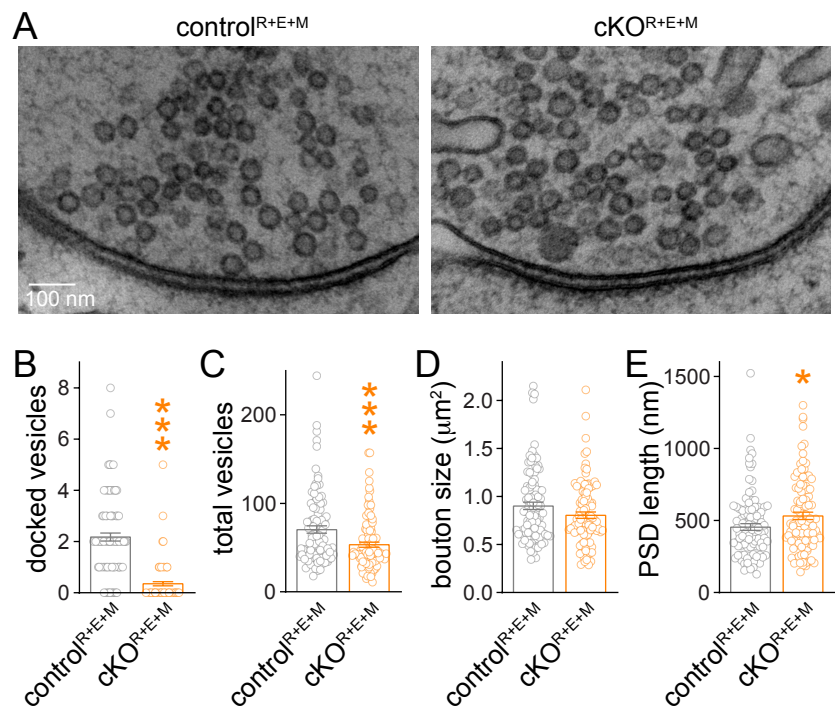
1018



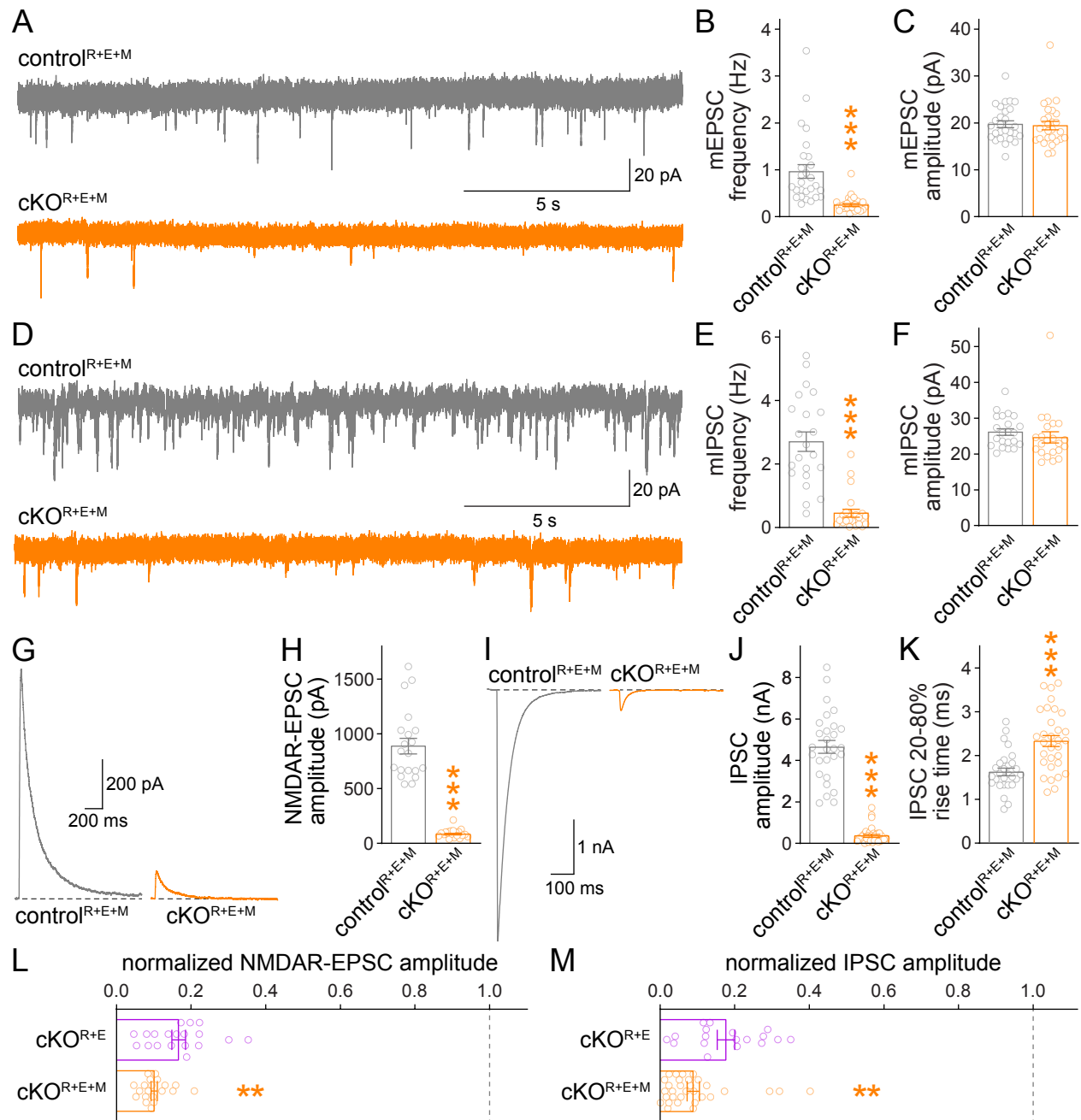
Tan et al., Figure 1



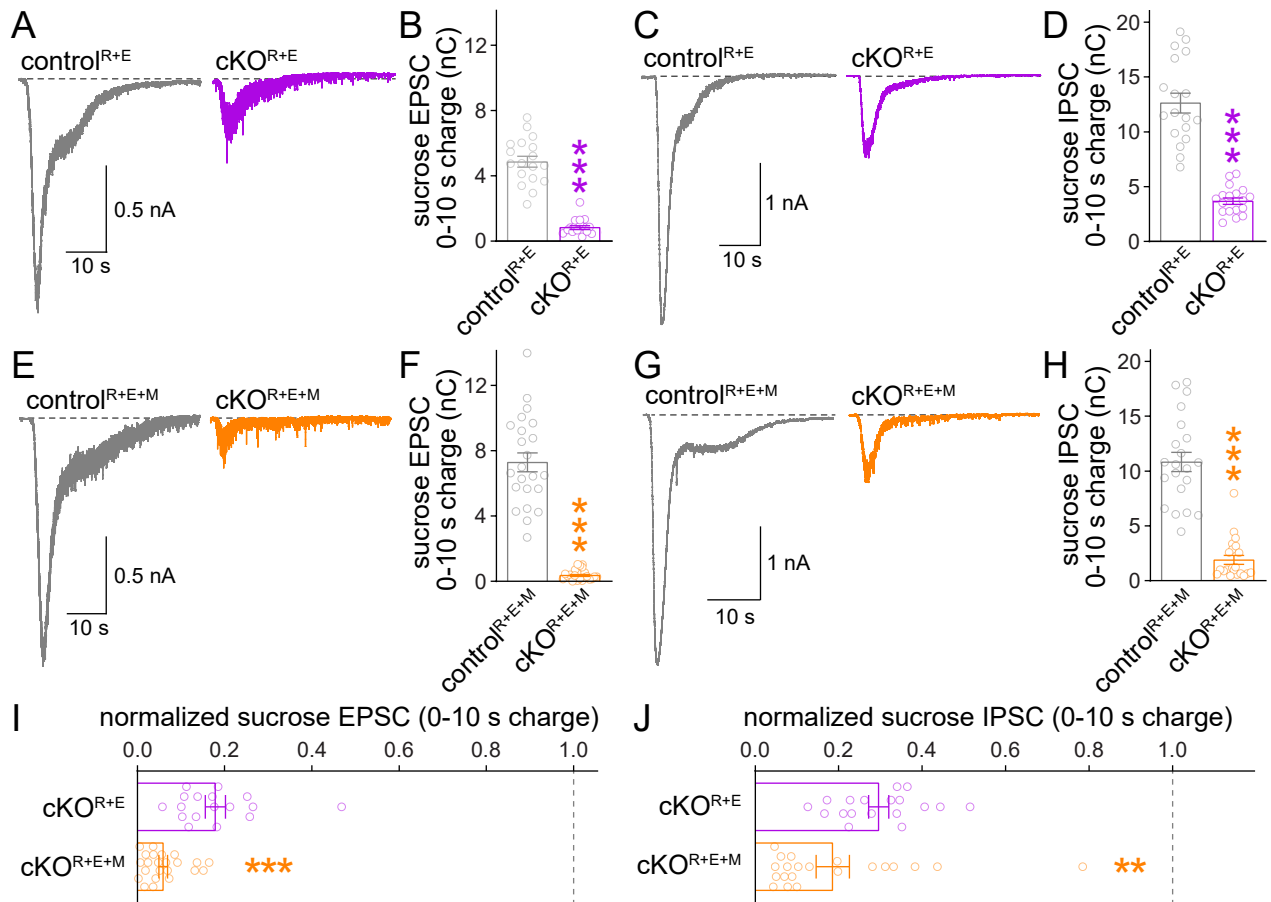
Tan et al., Figure 2



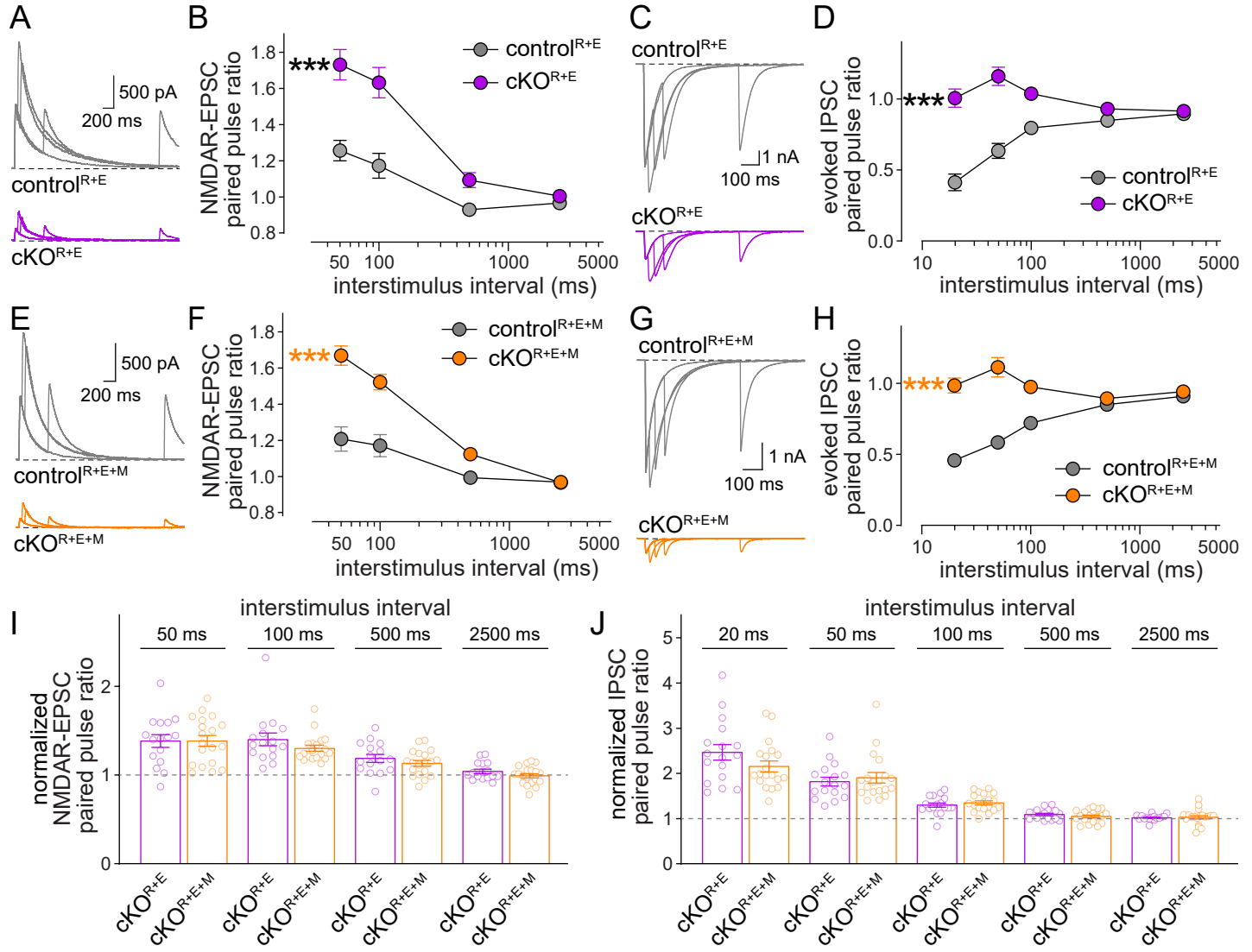
Tan et al., Figure 3



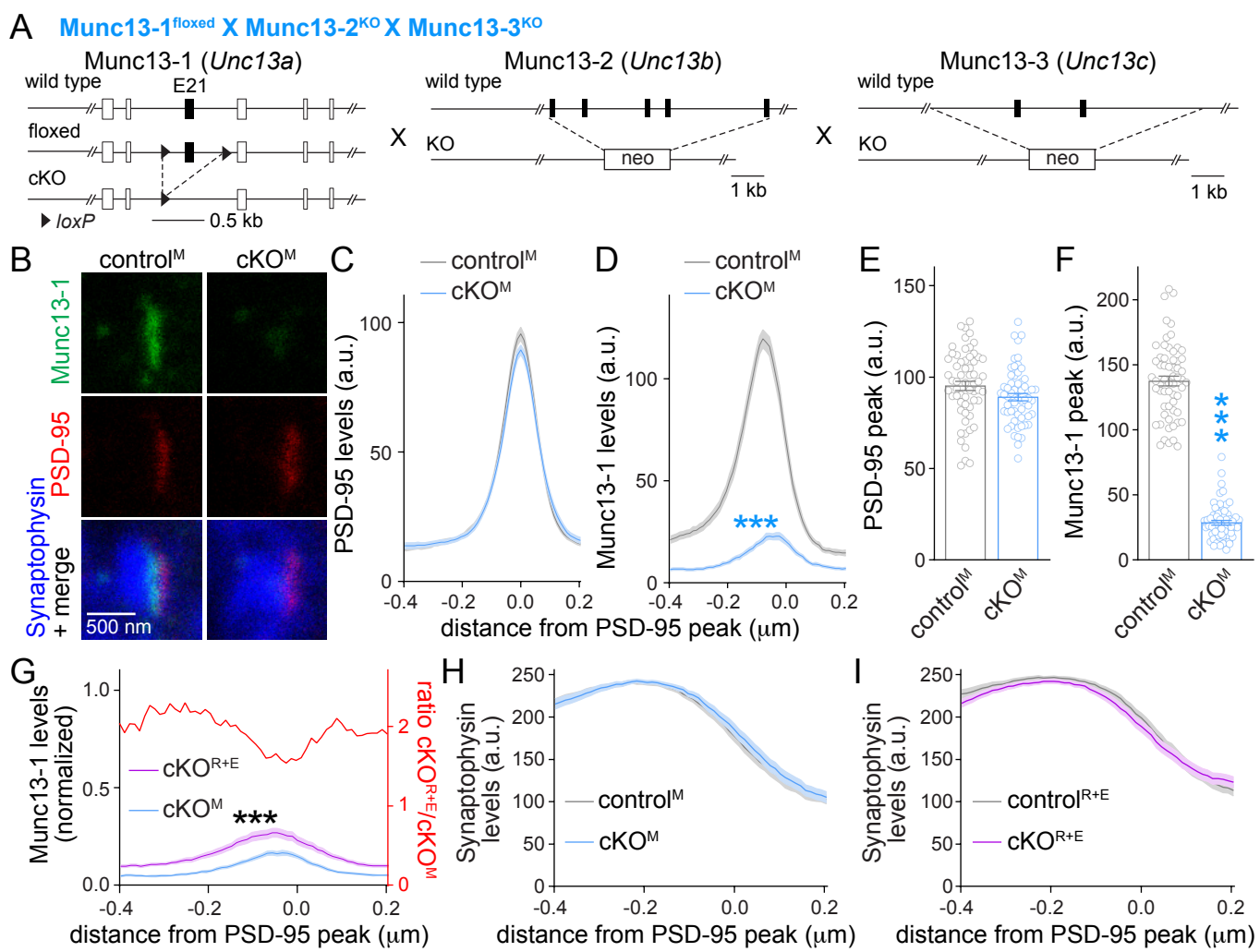
Tan et al., Figure 4



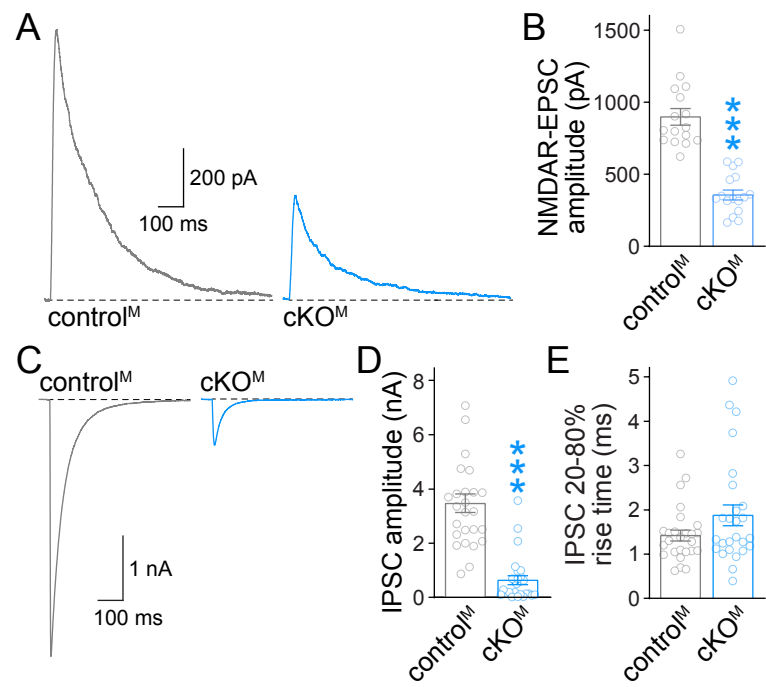
Tan et al., Figure 5



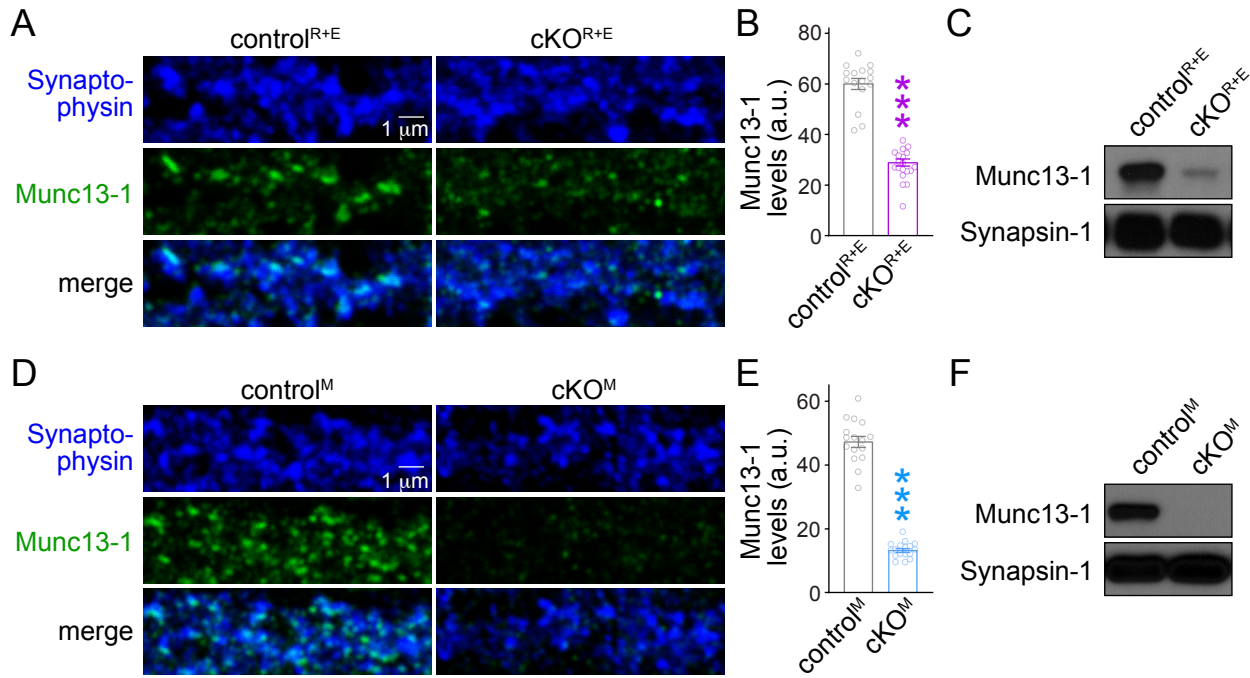
Tan et al., Figure 6



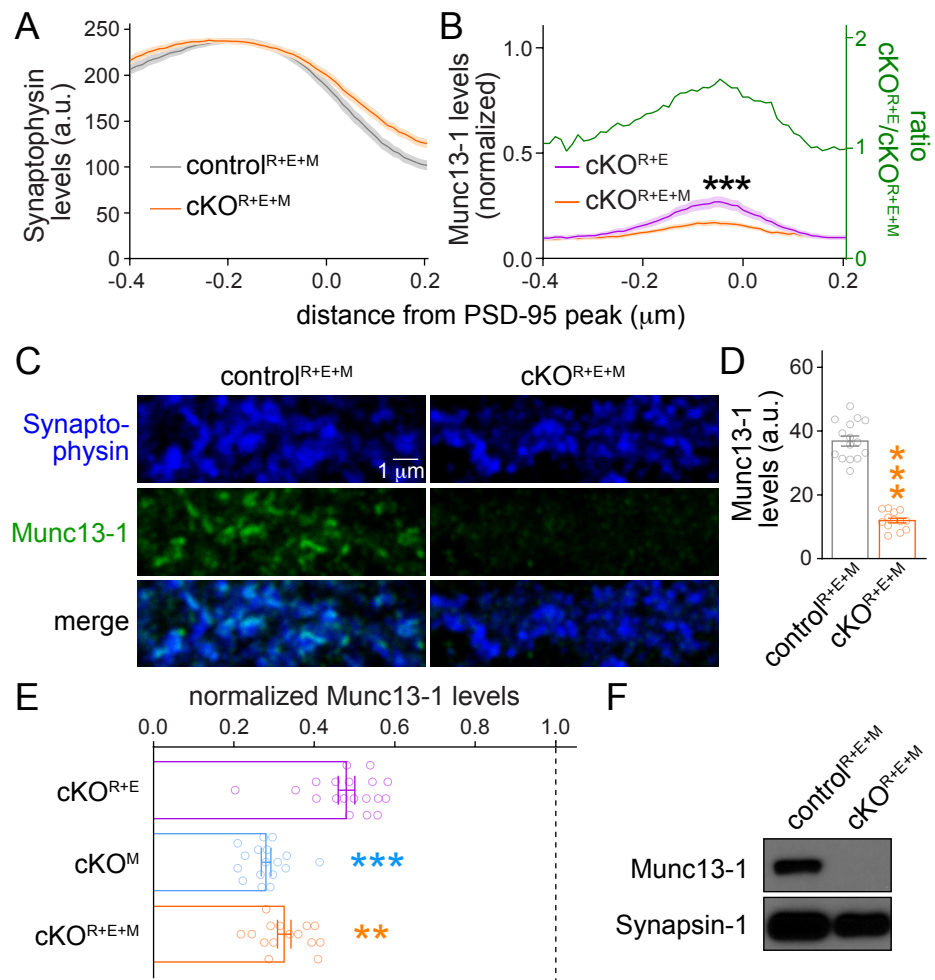
Tan et al., Figure 1 - figure supplement 1



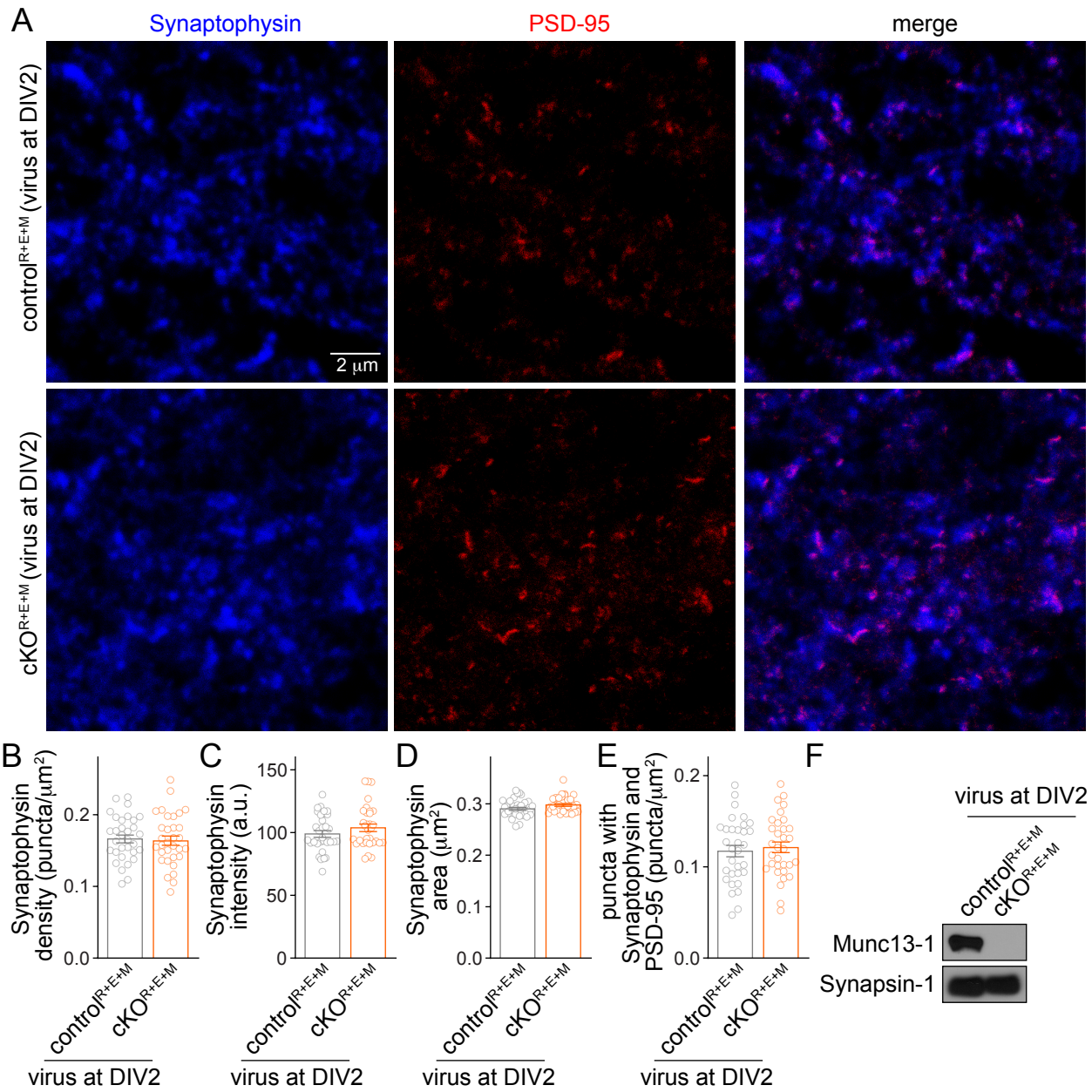
Tan et al., Figure 1- figure supplement 2



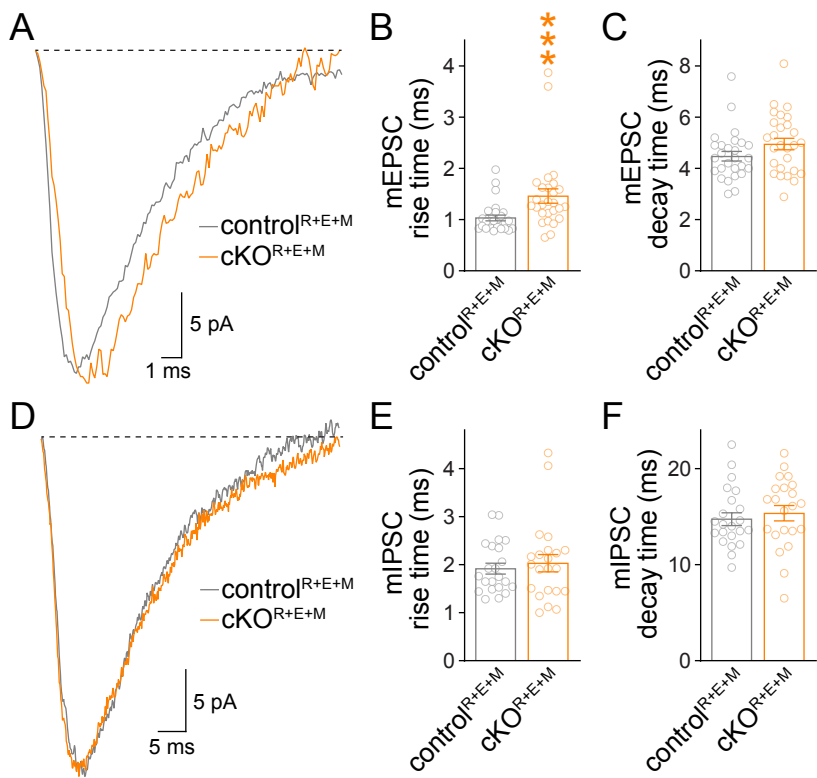
Tan et al., Figure 1 - figure supplement 3



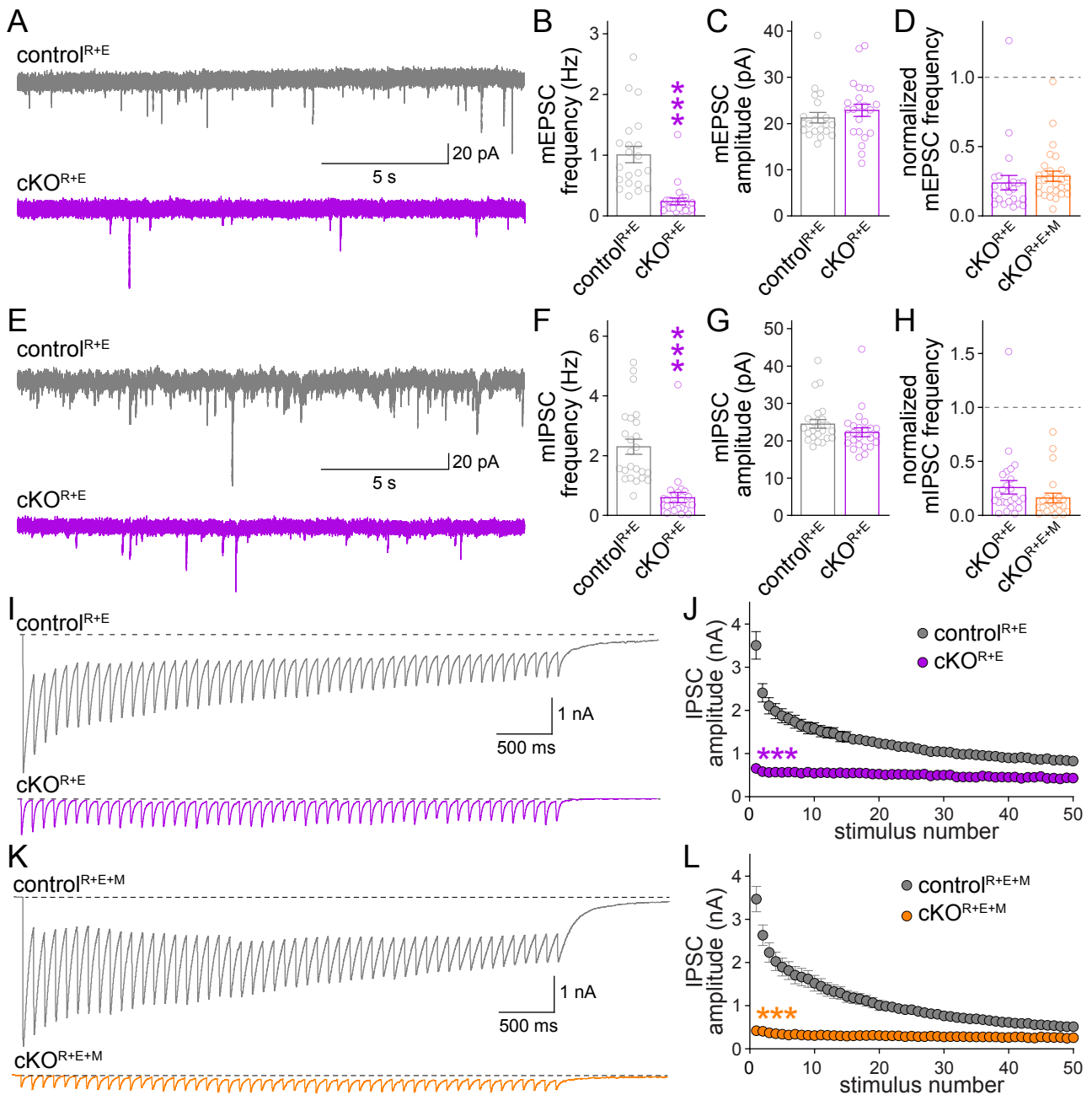
Tan et al., Figure 2 - figure supplement 1



Tan et al., Figure 2 - figure supplement 2



Tan et al., Figure 4 - figure supplement 1



Tan et al., Figure 6 - figure supplement 1